



A variational scheme for retrieving ice cloud properties from combined radar, lidar, and infrared radiometer

Julien Delanoë¹ and Robin J. Hogan¹

Received 23 May 2007; revised 18 October 2007; accepted 5 December 2007; published 9 April 2008.

[1] A variational method is described for retrieving profiles of visible extinction coefficient, ice water content and effective radius in ice clouds using the combination of ground-based or spaceborne radar, lidar and infrared radiometer. The forward model includes effects such as non-Rayleigh scattering by the radar and molecular and multiple scattering by the lidar. By rigorous treatment of errors and a careful choice of state variables and associated a priori estimates, a seamless retrieval is possible between regions of the cloud detected by both radar and lidar and regions detected by just one of these two instruments. Thus, when the lidar signal is unavailable (for reasons such as strong attenuation), the retrieval tends toward an empirical relationship using radar reflectivity factor and temperature, and when the radar signal is unavailable (such as in optically thin cirrus), accurate retrievals are still possible from the combination of lidar and radiometer. The method is tested first on simulated profiles from aircraft data and then on real observations taken in West Africa. It would be straightforward to expand the approach to include other measurements simply by including a forward model for them.

Citation: Delanoë, J., and R. J. Hogan (2008), A variational scheme for retrieving ice cloud properties from combined radar, lidar, and infrared radiometer, *J. Geophys. Res.*, *113*, D07204, doi:10.1029/2007JD009000.

1. Introduction

[2] It is widely recognized that clouds play an important role in both weather and climate forecasts [Stephens, 2005]. Since there remains a lack of information regarding the properties of clouds globally, cloud radars, lidars and radiometers have been installed at a number of sites worldwide [Stokes and Schwartz, 1994; Illingworth *et al.*, 2007] with the aim of monitoring the microphysical and radiative properties of clouds. This has recently been extended to space with the “A-Train” of satellites, comprising the cloud radar CloudSat [Stephens *et al.*, 2002], the lidar CALIPSO (Cloud Aerosol Lidar and Infrared Pathfinder Satellite Observations; [Winker *et al.*, 2003]) and a large number of radiometers, particularly on the Aqua satellite. The challenge is to use the synergy of radar, lidar and radiometers to retrieve the cloud water content, visible extinction coefficient and effective radius, from space or the ground.

[3] In this paper we propose a variational method that can use all the available measurements to retrieve the properties of ice clouds. A number of previous radar-lidar algorithms have been proposed for ice clouds. The first was by Intrieri *et al.* [1993] but this was limited to very optically thin clouds since the effects of lidar attenuation were neglected.

More recently, Wang and Sassen [2002], Okamoto *et al.* [2003] and Mitrescu *et al.* [2005] included a correction for lidar attenuation, but a value for the lidar extinction-to-backscatter ratio had to be assumed. A difficulty with this approach is that the retrieved extinction is very dependent on the exact value that is assumed, tending to make the retrievals increasingly inaccurate as they penetrate further into the cloud.

[4] A solution to this problem was provided by Donovan *et al.* [2001] and Tinel *et al.* [2005], who used the radar signal to assist in the correction for lidar attenuation. It was demonstrated by Hogan *et al.* [2006a] that these approaches are both able to retrieve accurate visible extinction coefficient, α_v , without specifying the extinction-to-backscatter ratio. Indeed, the retrieval of α_v was found to be independent of the microphysical assumptions that were made (e.g., the density-diameter and area-diameter relationships). This is a very convenient property since this variable is of foremost importance in determining the way the cloud interacts with natural radiation. The microphysical assumptions do have an effect on the retrieved ice water content and effective radius, and the assumptions made in a number of different algorithms were compared by Heymsfield *et al.* [2008].

[5] The current radar-lidar methods suffer from the following limitations: (1) They only work in regions where clouds are detected by both radar and lidar; the many regions of cloud detected by only one instrument are omitted, which is inconvenient when building a cloud climatology [Illingworth *et al.*, 2007]. (2) Noise in measure-

¹Department of Meteorology, University of Reading, Reading, UK.

ments results in noise in the retrieved variables. (3) Because of the architecture of these algorithms it is often not possible to make use of other measurements, such as radiances, Doppler velocity, or lidar molecular scattering beyond the cloud which provides an optical depth constraint. (4) It is difficult to also retrieve the properties of liquid clouds in the profile in a consistent fashion, particularly if they are embedded within the ice cloud. (5) Often there is a difficulty in incorporating the effects of lidar multiple scattering, and the widely used lidar multiple-scattering model of *Eloranta* [1998] is too slow to take to greater than third- or fourth-order scattering in operational algorithms for spaceborne instruments.

[6] In this paper we propose to address these limitations using a variational scheme (also referred to as “Bayesian,” or based on “optimal estimation theory” [Rodgers, 2000]). This is a very powerful tool in satellite retrievals and has recently been applied to active instruments [e.g., *Austin and Stephens*, 2001; *Löhnert et al.*, 2004; *Mitrescu et al.*, 2005; *Hogan*, 2007].

[7] The structure of the paper is as follows. In section 2, the new radar-lidar-radiometer method is described, including the relevant background about optimal estimation theory. A key component of this scheme is accurate and fast forward models for each of the instruments, as described in section 3. In section 4, the method is tested on synthetic radar and lidar profiles, and then in section 5 it is applied to a real ice cloud sampled over Niamey in West Africa. Prospects for application to A-Train and other data will then be discussed in section 6.

2. Retrieval Method

2.1. Overview

[8] This retrieval combines active and passive remote sensing instruments, in particular radar, lidar and Infrared radiometer, to estimate the properties of ice clouds. We assume that all instruments have been calibrated, that the nature of the random errors in the measurements is known, and that the radar and lidar are coordinated such that they are observing the same column of the atmosphere (see section 3.7 for discussion of the consequences of mismatched fields of view). Profiles are analyzed in turn, and the procedures undertaken for each are summarized in Figure 1.

[9] The first task (indicated by box 1 in Figure 1) is to classify the nature of the targets as a function of height into liquid droplets, ice particles, aerosol, insects, melting ice, rain, and combinations thereof. A method for doing this from ground-based data as part of “Cloudnet” was described by *Hogan and O’Connor* [2006] and *Illingworth et al.* [2007].

[10] The retrieval is then applied to the parts of the profile containing ice cloud. The algorithm described here is restricted to ice clouds that are unobscured by liquid clouds as far as the radar and lidar are concerned. Furthermore, when liquid clouds are present at any height in the profile, the Infrared radiometer observations are not used. Work is in progress to remove these restrictions and to retrieve the properties of ice clouds, liquid clouds, aerosol layers and precipitation within the same variational framework.

[11] In a variational scheme, one must decide what variables to use to describe the system being observed. These variables will be retrieved and are represented as the state vector, \mathbf{x} . In the case of ice clouds, the visible extinction coefficient, α_v , has the advantage that, in the geometric optics limit, it is directly linked to the both the lidar measurements and to the optical depth of the cloud. For example, in the single-scattering limit and in the absence of molecular scattering, the apparent lidar backscatter a range r from the instrument can be expressed as

$$\beta(r) = \hat{\beta}(r) \exp\left[-2 \int_0^r \alpha_v(r') dr'\right], \quad (1)$$

where $\hat{\beta}$ is “true” lidar backscatter coefficient, assumed proportional to α_v via the extinction-to-backscatter ratio, S :

$$\hat{\beta} = \alpha_v/S. \quad (2)$$

Hence the second variable to be added to the state vector is S . In common with *Donovan et al.* [2001] and *Tinel et al.* [2005], this variable is assumed constant with height, for the simple reason that without an independent measure of α_v (e.g., from a Raman or high spectral resolution lidar), we have no information on its height dependence. This was shown by *Hogan et al.* [2006a] to cause only modest errors in the retrieved α_v . In practice, (1) is replaced by a formulation including molecular and multiple scattering, as described in section 3.4.

[12] In order to relate α_v to other moments of the size distribution such as radar reflectivity factor (Z) or ice water content (IWC), it needs to be supplemented in the state vector by another intensive or extensive variable, such as a measure of particle size or number concentration. This additional variable should ideally have two key properties. Firstly, a good a priori estimate of it should be available as a function of temperature. This ensures that in regions where only the radar or the lidar is available, the scheme will tend toward existing empirical relationships involving temperature, such as the formulae for IWC as a function of Z and temperature [e.g., *Liu and Illingworth*, 2000; *Hogan et al.*, 2006b; *Protat et al.*, 2007]. It was demonstrated by *Hogan et al.* [2006b] that the temperature dependence in these relationships must arise via the temperature dependence of the number concentration parameter of a size distribution, commonly referred to as N_0 . Secondly, it should be easy to combine this additional variable with α_v to estimate any other property of the size distribution. A good candidate is the ice normalized number concentration parameter, N_0^* ; it was shown by *Delanoë et al.* [2005] and *Field et al.* [2005] that for any intensive variable y and extensive variable Y there is a near-unique relationship between the ratio α_v/N_0^* and both y and the ratio Y/N_0^* .

[13] Given these requirements, the last variable we add to the state vector is N_0' , defined as

$$N_0' = N_0^*/\alpha_v^{0.6}. \quad (3)$$

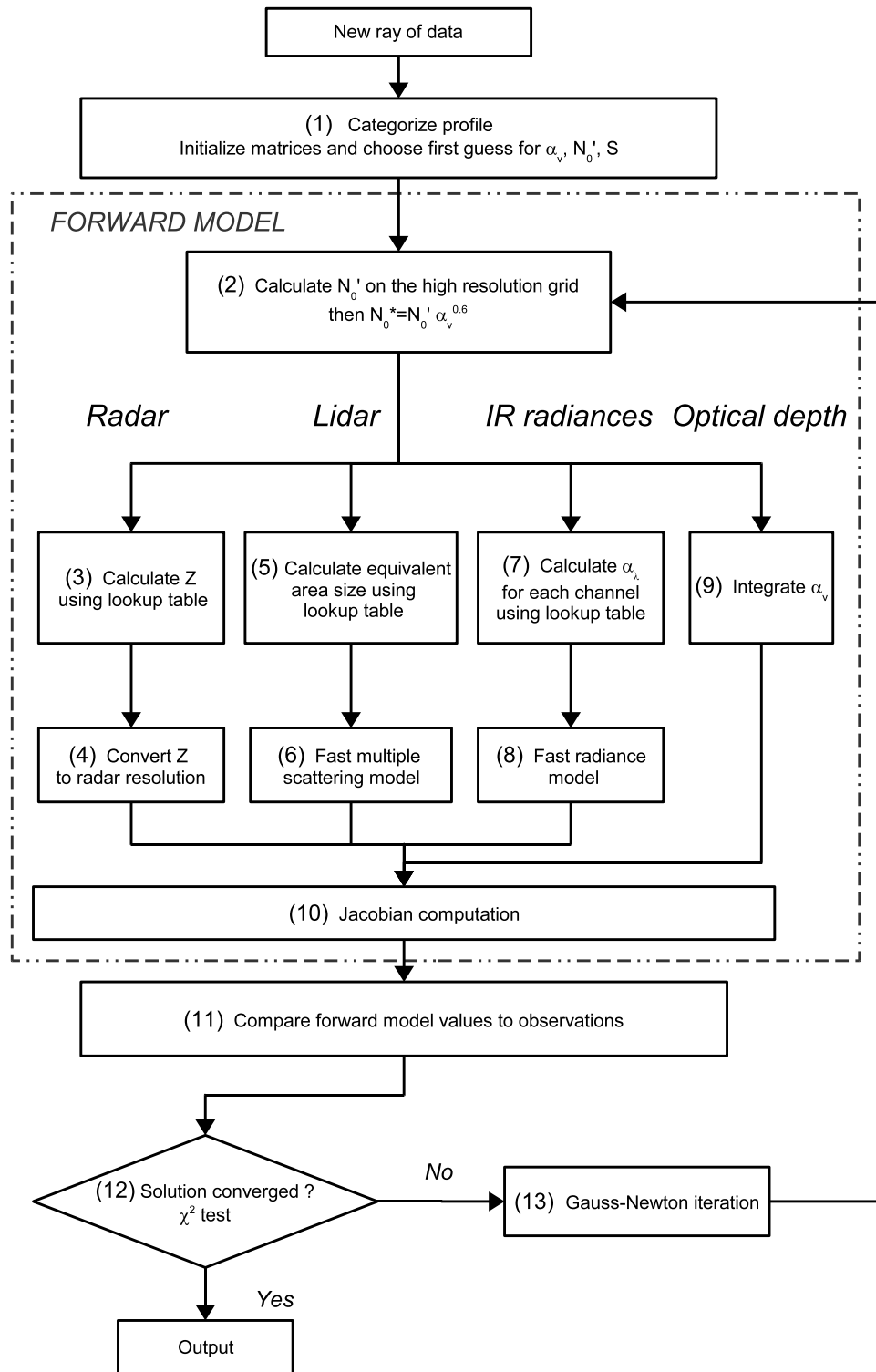


Figure 1. Flowchart showing the sequence of operations performed by the retrieval scheme. The detailed description of each step is given in sections 2 and 3.

As shown in section 3.2, this variable is found to have a strong temperature dependence. Furthermore, N_0^* can easily be derived from the combination of α_v and N_0' , which then enables any intensive or extensive variable to be estimated (see section 3.1).

[14] To improve the computational efficiency, we seek to reduce the number of elements in \mathbf{x} . Naturally, α_v is only retrieved at the n ranges where ice cloud is detected by either the radar or the lidar. An additional efficiency is obtained by not retrieving N_0' directly at each gate, but rather representing it by reduced set of m basis functions,

N_b , such that smooth variation in range is guaranteed. The same approach was used by Hogan [2007] to retrieve an analogous variable for polarization radar in rain. Consequently, the state vector for a single profile is

$$\mathbf{x} = \begin{pmatrix} \ln \alpha_{v,1} \\ \vdots \\ \ln \alpha_{v,n} \\ \ln S \\ \ln N_{b,1} \\ \vdots \\ \ln N_{b,m} \end{pmatrix}. \quad (4)$$

Note that we use the logarithm of the entities α_v , N_b and S , not the entities themselves, to avoid the unphysical possibility of retrieving negative values.

[15] With the state vector now defined, we turn to the observation vector, \mathbf{y} . This contains the measurements Z (the radar reflectivity factor), β (the apparent lidar backscatter), I_λ (the Infrared radiance at wavelength λ) and ΔI (the difference between two Infrared radiances). Radiances measured in the Infrared atmospheric window provide information on the extinction of the cloud within the nearest one or two optical depths, provided that the temperature profile is well known. The combination of ground-based radar and Infrared radiometer was used by Matrosov *et al.* [1994] to retrieve the properties of ice clouds, but here we consider Infrared radiances measured by satellite in combination with either ground-based or spaceborne radar and lidar. The difference between two infrared radiances provides information on ice particle size [Chiriaco *et al.*, 2004; Cooper *et al.*, 2003].

[16] In daylight hours, information on cloud visible optical depth δ_v is available from shortwave radiances measured by satellite instruments. In practice, it can be rather difficult to model such radiances directly because of three-dimensional radiative effects [Várnai and Marshak, 2001] and (in the case of A-Train retrievals) the need to know the spectrally dependent bidirectional reflection function of the surface at all points on the globe. We therefore follow the example of Benedetti *et al.* [2003a] and Mitrescu *et al.* [2005] and include in the formalism a way to include an independent retrieval of δ_v (e.g., derived using the method of Platnick *et al.* [2003]) as if it were a direct observation with an associated error.

[17] Hence, the observation vector can be written as

$$\mathbf{y} = \begin{pmatrix} \ln \beta_1 \\ \vdots \\ \ln \beta_p \\ \ln Z_1 \\ \vdots \\ \ln Z_q \\ I_\lambda \\ \Delta I \\ \delta_v \end{pmatrix}. \quad (5)$$

Note that β and Z need not be on the same grid, as shown by the different indices p and q . Moreover, in the case of the lidar signal it is advantageous to include in \mathbf{y} any gates beyond the far end of the cloud. This enables any molecular return measured here to be used automatically as a constraint on optical depth [Cadet *et al.*, 2005]. If measurements are missing they are simply excluded from \mathbf{y} . As in the state vector, the logarithms of the entities β and Z are used because of the large dynamic range that they can span in a single profile. It is also found that the use of logarithms in \mathbf{x} and \mathbf{y} results in much faster convergence to the correct solution.

2.2. Optimal Estimation Formulation

[18] The essence of the technique is to start with a first guess of the state vector and use a forward model (represented by the dot-dashed box in Figure 1 and described in section 3) to predict each element of the observation vector. This prediction is compared to the actual observations (box 11 of Figure 1) and the difference is used to calculate a refined state vector that is fed back into the forward model. This process is repeated until convergence. The aim is to find the state vector that minimizes the difference between the observations and the forward model in a least-squares sense. This is achieved by minimizing a cost function J :

$$2J = \sum_{i=1}^q \frac{(\ln Z_i - \ln Z'_i)^2}{\sigma_{\ln Z_i}^2} + \sum_{i=1}^p \frac{(\ln \beta_i - \ln \beta'_i)^2}{\sigma_{\ln \beta_i}^2} + \frac{(\delta_v - \delta'_v)^2}{\sigma_{\delta_v}^2} + \frac{(I_\lambda - I'_\lambda)^2}{\sigma_{I_\lambda}^2} + \frac{(\Delta I - \Delta I')^2}{\sigma_{\Delta I}^2} + \sum_{i=1}^{n+m+1} \frac{(x_i - x_i^a)^2}{\sigma_{a,i}^2}. \quad (6)$$

The first five elements on the right hand side of (6) represent the deviation of the observations $\ln Z$, $\ln \beta$, I_λ , ΔI and δ_v , from the values predicted by the forward model $\ln Z'$, $\ln \beta'$, I'_λ , $\Delta I'$ and δ'_v , with the root-mean-squared (RMS) observational errors represented by $\sigma_{\ln Z}$, $\sigma_{\ln \beta}$, σ_{I_λ} , $\sigma_{\Delta I}$ and σ_{δ_v} . In practice these include forward model errors as discussed in sections 2.5 and 3.7.

[19] The last summation in (6) represents the deviation of the elements of the state vector from some a priori estimate, x^a (referred to as the ‘‘background’’ in data assimilation). This term assists in the stability of the algorithm and ensures that if radar or lidar observations are missing then the retrieval will tend toward the behavior of existing empirical algorithms in the literature. In practice, an a priori is only required for N'_0 (see section 3.2) and S , not for α_v . A wide range of values of S have been reported in the literature; following the evidence of Platt *et al.* [1987] and Chen *et al.* [2002] of S typically varying between 20 sr and 50 sr, we assume an a priori of $\ln S = 3.5 \pm 0.5$ sr. An a priori for visible extinction coefficient is not required since this variable is well constrained by both radar and lidar; therefore, the corresponding term is simply omitted from the cost function. In any case, extinction has a large variability in nature so any a priori would be have to be

The top left $(n + 1) \times (n + 1)$ elements of \mathbf{W} correspond to the α_v and S elements of \mathbf{x} that are unchanged by the transformation, so are represented in \mathbf{W} by an identity matrix. The bottom right $n \times m$ elements of \mathbf{W} contain the basis functions. Following Hogan [2007], we use cubic spline basis functions, resulting in the retrieved N_0' being continuous in itself and its first and second derivatives. Details of how to set these elements of \mathbf{W} may be found in the appendix of Hogan [2007]. The Jacobian that is output from the forward model, $\hat{\mathbf{H}}$, is also on the lidar range grid; that is, it consists of derivatives with respect to N_0' rather than the corresponding basis function amplitudes N_b . We convert this high-resolution Jacobian to the standard Jacobian used at the basis function resolution by simply postmultiplying by \mathbf{W} :

$$\mathbf{H} = \hat{\mathbf{H}}\mathbf{W}. \quad (13)$$

2.4. Use of a Priori Error Covariances for Spreading of Number Concentration Information in Height

[26] As described in section 3.2, an N_0' -temperature relationship is used as an a priori constraint on N_0' . Physically, this can be thought of as expressing the fact that lower down in a cloud (i.e., at warmer temperatures), the process of aggregation leads to a smaller number of larger particles. Algorithmically, this ensures that the N_0' retrieved by the scheme tends toward a physical value when only one instrument is available. In the simplest case, the \mathbf{B} matrix is diagonal and the diagonal elements are the error variances of the a priori estimate \mathbf{x}^a , i.e., $B_{i,i} = \sigma_a^2$ (see section 3.2 for the value used).

[27] Very often in spaceborne radar-lidar retrievals, within a single profile we have a region of cloud detected by both radar and lidar, above which is a region detected by lidar alone and below which is a region detected by radar alone. In this case, if \mathbf{B} is diagonal, the retrieved N_0' would be determined closely by the radar and lidar in the region where both detect the cloud, but within the height span of a single basis function, would switch back to a value much closer to the a priori in the regions detected by just one instrument.

[28] A more realistic retrieval would take account of the fact that, if in the radar-lidar region the retrieved N_0' is higher than the a priori estimate, then we would expect it to be higher in the radar-only and lidar-only regions as well. This tendency is implemented via the off-diagonal elements of \mathbf{B} , which express the fact that the difference between the actual value of N_0' and the a priori value is spatially correlated. Following Hogan [2007], if we assume that the correlation coefficient between two basis function coefficients centered at heights z_i and z_j decreases as an inverse exponential with the separation distance, then the off-diagonal covariance terms of \mathbf{B} are given by

$$B_{i,j} = B_{i,i} \exp(-|z_j - z_i|/z_0), \quad (14)$$

where z_0 is the decorrelation distance and it has been assumed that σ_a^2 is constant with height.

[29] Note that an a priori is only used for N_0' and S , so (14) only applies to the N_0' part of \mathbf{B} . As yet, there is no observational data to choose a particularly value of z_0 , a problem common to many areas of data assimilation [Daley, 1991]. In principle this parameter could be estimated from a large number of profiles of N_0' derived where both Z and β are available using the method of Hollingsworth and Lönnberg [1986]. In the remainder of this paper a value of $z_0 = 1$ km is used.

2.5. Calculation of the Retrieval Error

[30] After the solution has converged, the error covariance matrix, \mathbf{S}_x , of the retrieved variables held in the state vector is simply given by the inverse of the Hessian matrix, i.e., $\mathbf{S}_x = \mathbf{A}^{-1}$ [Rodgers, 2000]. Hence, the first n diagonal terms of \mathbf{S}_x represent the error variances in $\ln \alpha_v$, with the remainder representing error variances in $\ln S$ and $\ln N_b$. The error covariance matrix of the high-resolution transformation of the state vector $\hat{\mathbf{x}}$ defined in (12) is given by premultiplying and postmultiplying by the weighting function matrix \mathbf{W} :

$$\mathbf{S}_{\hat{\mathbf{x}}} = \mathbf{W}^T \mathbf{S}_x \mathbf{W}. \quad (15)$$

The final n diagonal elements of $\mathbf{S}_{\hat{\mathbf{x}}}$ represent the error variances of N_0' at the same resolution as α_v . Errors in any other microphysical variables derived from α_v and N_0' (in particular IWC and r_e) may be calculated from $\mathbf{S}_{\hat{\mathbf{x}}}$, as described in Appendix A.

[31] It should be stressed that the retrieval errors obtained in this way depend strongly on the observational errors that are assigned in (6). For the retrieval error to be realistic it is important that the observational errors include the error in the forward model. Formally we may write that the observation error covariance matrix is given by $\mathbf{R} = \mathbf{O} + \mathbf{M}$, where \mathbf{O} is the error covariance solely due to instrumental error and \mathbf{M} is the forward model error. Discussion of the error associated with each component of the forward model is given in section 3.7.

3. Forward Model

[32] In this section, the forward model $H(\mathbf{x})$ used in the scheme is described. As stated before, the forward model produces an estimate of the observations \mathbf{y} from the state vector \mathbf{x} , and is represented in Figure 1 by the dot-dashed box. Readers who are familiar with the interpretation of microphysical cloud properties and instrumental parameters may wish to skip some or all of this section.

[33] In addition to the information held within the state vector, a large amount of ancillary information is required for each of the components of the forward model. This includes the thermodynamic state of the atmosphere (in particular, profiles of temperature, pressure, humidity and ozone concentration), the properties of the surface (skin temperature and emissivity at the radiometer wavelengths), as well as the properties of the instruments themselves (in particular the lidar field of view to calculate the contribution from multiple scattering). Such information can be obtained with adequate accuracy from standard analysis and forecast products that are archived with both ground-based Cloudnet data and within the CloudSat database.

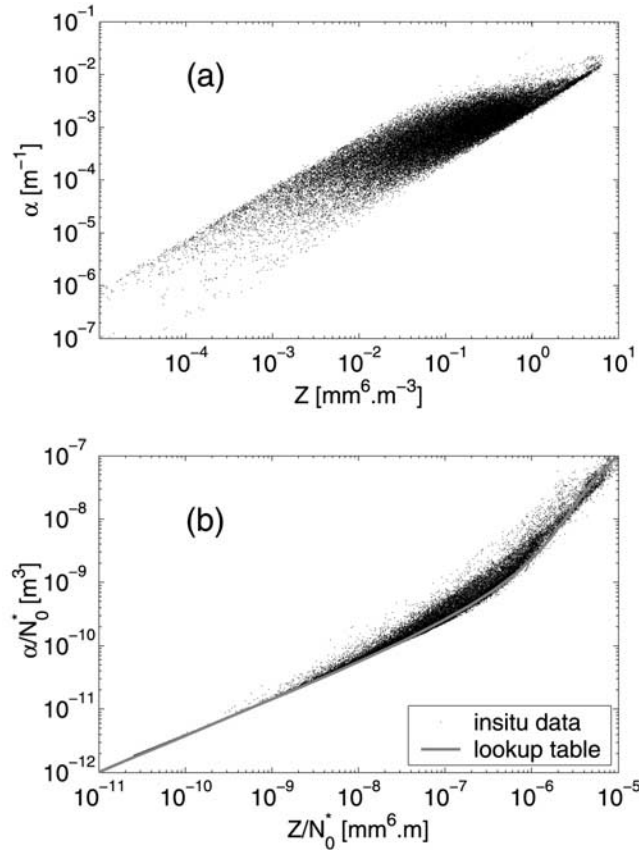


Figure 2. (a) Visible extinction coefficient α_v , as a function of 94-GHz radar reflectivity factor Z for the large in situ aircraft database of *Delanoë et al.* [2005]. (b) The same but after dividing both variables by the normalized number concentration parameter N_0^* . The gray line corresponds to the fit calculated using the unified size distribution shape of *Field et al.* [2005]. The curved shape in the relationship is due to the transition between Rayleigh scattering at small particle sizes to Mie scattering at larger sizes.

3.1. Normalized Concentration Parameter N_0^* and the Look-Up Tables

[34] Nearly all components of the forward model require the ability to predict arbitrary intensive and extensive variables from the combination of α_v and N_0' . This is achieved by first calculating N_0^* using (3), then using one-dimensional look-up tables to relate the ratio α_v/N_0^* to either an intensive variable y , or to Y/N_0^* , where Y is an extensive variable. In this section it will be shown how these look-up tables are generated, highlighting the strength of the N_0^* concept.

[35] First, we need to decide on a microphysical model, describing the shape of the particle size distribution and the relationships between particle mass, cross-sectional area and size. The distributions are formulated in terms of the maximum particle dimension, D . The ice particle mass is assumed to follow the *Brown and Francis* [1995] mass- D relationship, which was found by *Hogan et al.* [2006b] to be accurate when calculating Z from aircraft data in midlatitude

ice clouds. The corresponding area-size relationship is taken from *Francis et al.* [1998], who used the same aircraft data set as *Brown and Francis* [1995]. Adopting the formalism of *Delanoë et al.* [2005] and *Field et al.* [2005], we describe the size distribution as

$$N(D) = N_0^* F(D/D_0^*), \quad (16)$$

where N_0^* is the normalized number concentration parameter, given by

$$N_0^* = M_2^4/M_3^3, \quad (17)$$

and M_n is the n th moment of the ice particle size distribution. Particle size in (16) is normalized by D_0^* , a measure of the mean size of the distribution and defined as

$$D_0^* = M_3/M_2. \quad (18)$$

The function F in (16) is the “unified” size distribution shape given by *Field et al.* [2005], and has been found to fit measured size distributions when they are appropriately normalized (i.e., F fits N/N_0^* versus D/D_0^*).

[36] To generate the look-up tables, we cycle through a wide range of values of D_0^* and for each calculate α_v/N_0^* , y and Y/N_0^* (where y and Y represent all intensive and extensive variables of interest). Geometric optics is used to calculate α_v via the area-size relationship discussed above. In the case when Y represents radar reflectivity factor Z , Mie theory is applied assuming the particles to be homogeneous ice-air spheres of diameter D and mass m . Similarly, the ice water content, IWC, is simply the integrated particle mass across the size distribution. The intensive variable effective radius, r_e , is derived using [*Foot, 1988*]

$$r_e = \frac{3}{2} \frac{\text{IWC}}{\alpha_v \rho_i}, \quad (19)$$

where ρ_i is the density of solid ice. Other variables are derived in a similar fashion.

[37] To demonstrate the strength of this approach, Figure 2a shows α_v as a function of 94-GHz Z derived from the same large in situ aircraft database used by *Delanoë et al.* [2005] and *Protat et al.* [2007]. There is clearly no unique relationship between the two variables, but Figure 2b shows that when both are normalized by N_0^* , the points collapse on to a much tighter curve. These observations are well fitted by the gray line, which indicates the look-up table derived using the unified size distribution shape discussed above. The same behavior is exhibited for all other extensive variables. Hence this can be used to predict Z and an other microphysical variables required in the forward model from the combination of α_v and N_0^* using one-dimensional look-up tables. In principle, any other pair of moments could be used to generate the required variables, but if one of them was not N_0^* then the look-up tables would have to be two-dimensional.

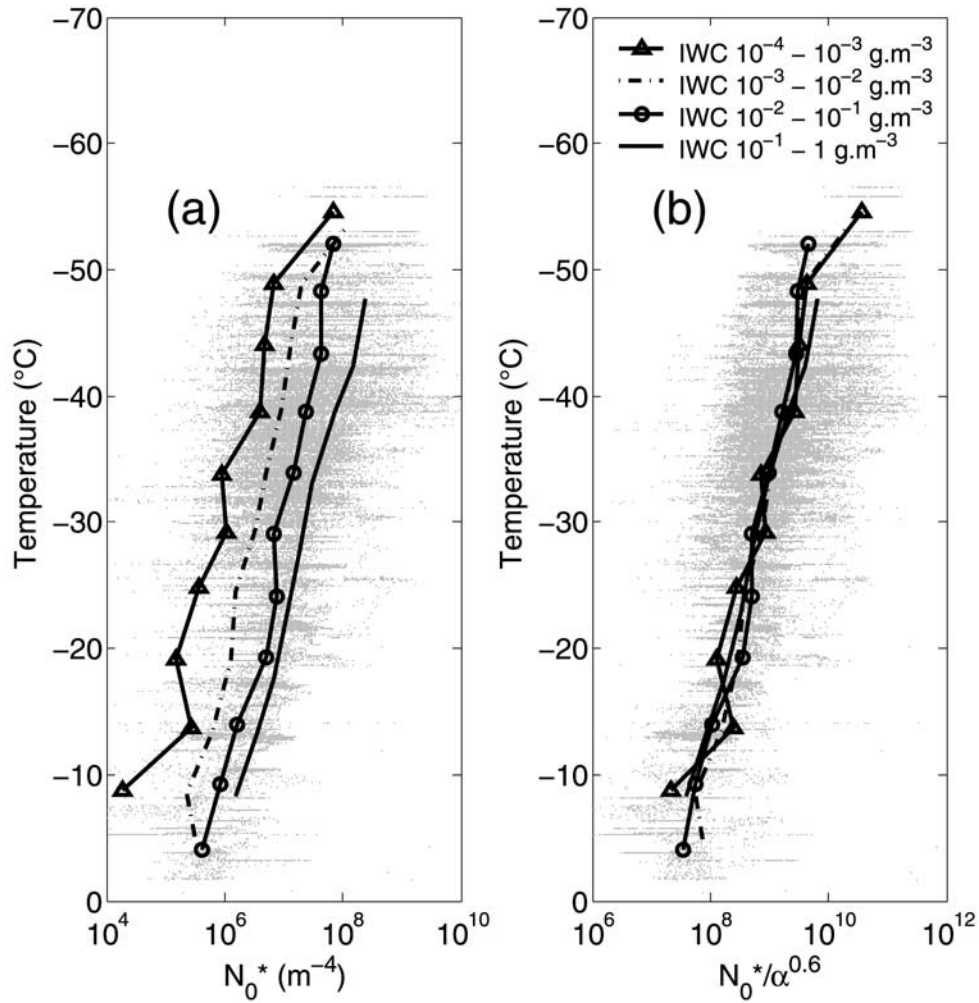


Figure 3. (a) The temperature dependence of N_0^* for each size distribution within the large in situ database of Delanoë *et al.* [2005] (dots), superimposed by the mean N_0^* in 5°C temperature ranges and various ranges of ice water content IWC (lines and symbols). (b) The same but for the variable $N_0' = N_0^*/\alpha^{0.6}$.

3.2. A Priori of the Normalized Concentration Parameter N_0'

[38] As discussed in section 2.1, a desirable property of at least one of the state variables is that we have a good a priori estimate of it from temperature (T), in order that when only the radar or the lidar are available, the retrieval is at least as accurate as existing empirical relationships based on temperature in the literature [e.g., Hogan *et al.*, 2006b].

[39] Figure 3a shows the temperature dependence of N_0^* using the same in situ database as used in Figure 2. It can be seen that, although there is such a relationship, it is not IWC independent. For both this reason, and in order to reduce the scatter, we divide it by a power of the visible extinction coefficient. A range of powers has been tested and it is found that the best results are found for a power of 0.6; Figure 3b clearly shows that there is an IWC-independent relationship between $N_0^*/\alpha^{0.6}$ and temperature. Hereafter this ratio will be represented by N_0' . Because a good a priori is available for N_0' , it is used in the state vector rather than N_0^* , but N_0^* needs to still be calculated as the first step

in the forward model (box 2 in Figure 1) before all the other variables can be calculated. The spread of the points in Figure 3b indicates that $\ln N_0'$ has a variance of 1.0, so this is the value used for the a priori error variance $B_{i,i}$ discussed in section 2.4.

3.3. Radar Forward Model

[40] The look-up tables calculated in section 3.1 are used in the forward model to derive Z from α_v and N_0^* , using the relationship between Z/N_0^* and α_v/N_0^* shown in Figure 2, and represented by box 3 in Figure 1. Gaseous attenuation at the radar wavelength is calculated using the look-up tables generated from the line-by-line model of Liebe [1985], coupled to estimated profiles of temperature, pressure and humidity as part of the ancillary data. Ice attenuation is believed to be small enough to be neglected [e.g., Hogan and Illingworth, 1999], and consideration of liquid water attenuation is avoided by restricting application of the retrieval to ice clouds unobscured by liquid layers. A future development of the scheme will be to include the retrieval of liquid water layers, in which case forward modeling of

the associated radar attenuation will be incorporated. In deep convective clouds observed by spaceborne radar, it has been shown that multiple scattering can be important [Battaglia *et al.*, 2007]. In such situations, a number of the assumptions made in this retrieval scheme would become inappropriate, particularly the use of the *Brown and Francis* [1995] mass-size relationship, which is suitable for low-density aggregates. However, in principle a fast radar multiple scattering model, such as the one of R. J. Hogan and A. Battaglia (Fast lidar and radar multiple-scattering models—2. Wide-angle scattering using the time-dependent two-stream approximation, submitted to *Journal of the Atmospheric Sciences*, 2007), could be incorporated.

[41] When the radar and lidar are on different range grids, α_v is retrieved at the resolution of the lidar, which is usually the higher resolution of the two (e.g., CALIPSO is available at a higher vertical resolution than CloudSat). Hence we need a way to convert Z derived from the look-up table to the radar observation grid, allowing for the possibility that the radar is oversampled in range. This is represented in Figure 1 by box 4 and is achieved using

$$\mathbf{y}_z = \mathbf{V}\hat{\mathbf{y}}_z, \quad (20)$$

where $\hat{\mathbf{y}}_z$ is a column vector containing the n high-resolution Z values, \mathbf{y}_z is a column vector containing the q values of Z on the radar grid, and \mathbf{V} is a precomputed $q \times n$ matrix that plays a similar role to the weighting function matrix in (12). To calculate the elements of \mathbf{V} , we assume that the radar has a Gaussian range-response function of RMS width σ_z . Hence the response function with height z for radar gate i is given by

$$V_i(z) = \frac{1}{\sqrt{2\pi}\sigma_z} \exp\left[-\frac{1}{2}\left(\frac{z-z_i}{\sigma_z}\right)^2\right], \quad (21)$$

normalized such that its integral with height is unity. To relate the radar reflectivity factor measured at gate i , Z_i , to the continuous field $Z(z)$, we have the convolution $Z_i = \int_0^\infty V_i(z)Z(z)dz$. If the continuous field is approximated by $\hat{\mathbf{y}}_z$, with the reflectivity factor at high-resolution gate j assumed to be constant between heights $z_{j-1/2}$ and $z_{j+1/2}$, then the elements of \mathbf{V} are given by

$$V_{i,j} = \int_{z_{j-1/2}}^{z_{j+1/2}} V_i(z)dz = \frac{1}{2} \left[\operatorname{erf}\left(\frac{z_{j+1/2}-z_i}{\sigma_z\sqrt{2}}\right) - \operatorname{erf}\left(\frac{z_{j-1/2}-z_i}{\sigma_z\sqrt{2}}\right) \right], \quad (22)$$

where erf denotes the error function. For computational efficiency, $V_{i,j}$ is set to zero when the heights of the boundaries of high-resolution gate j are more than $3\sigma_z$ from the center of radar gate i . The Jacobian of the radar forward model, i.e., the partial derivatives of $\ln Z$ at each gate with respect to $\ln \alpha_v$ and $\ln N_0'$, may be calculated efficiently using the gradient of the relevant look-up tables.

3.4. Lidar Multiple-Scattering Forward Model

[42] A very simple lidar forward model is provided by (1), but to include molecular scattering and multiple scattering,

we use the fast multiple-scattering model of *Hogan* [2006], which has been found to be as accurate as the widely used *Eloranta* [1998] model when taken to 5th order scattering, but is over 3 orders of magnitude faster for a 50-point profile. The model is represented by box 6 of Figure 1 and takes as input the lidar ratio S (assumed constant with height), and profiles of α_v and the “equivalent-area radius” r_a , i.e., the radius of a sphere with the same cross-sectional area as the mean area of the entire size distribution. A look-up table is used to convert α_v/N_0^* to r_a (box 5 of Figure 1). In order to estimate the molecular return, the profile of atmospheric density (calculated from temperature and pressure) is required. The model produces an estimate of the profile of apparent backscatter β , the separate returns from the cloud and the molecules (β^{clid} and β^{mol}), as well as the top left $p \times n$ part of the Jacobian \mathbf{H} in (9) that contains $\partial \ln \beta_i / \partial \ln \alpha_{v,j}$. An alternative method to calculate the Jacobian was provided by R. J. Hogan (Fast lidar and radar multiple-scattering models—1. Quasi-small-angle scattering using the photon variance-covariance method, submitted to *Journal of the Atmospheric Sciences*, 2007). Note that $\partial \ln \beta_i / \partial \ln \alpha_{v,j}$ is lower triangular in the sense that β_i only depends on values of $\alpha_{v,j}$ earlier in the profile, so values corresponding to $j > i$ are zero.

[43] We also require the elements of the Jacobian corresponding to the other terms in the state vector. The Jacobian with respect to the cloud extinction-to-backscatter ratio S is not affected by multiple scattering, and so from (1) and (2) it can be shown that in the absence of molecular scattering $\partial \ln \beta_i / \partial \ln S = -1$. When molecular scattering is included, we assume that the molecular extinction-to-backscatter ratio has a fixed value of $8\pi/3$ sr, and the Jacobian becomes $\partial \ln \beta_i / \partial \ln S = -\beta_i^{\text{clid}}/\beta_i$. The Jacobian with respect to N_0' arises because of the particle size dependence of multiple scattering. Since this is relatively weak, we assume that $\partial \ln \beta_i / \partial \ln N_{0,j} = 0$.

3.5. Infrared Radiance Forward Model

[44] For each infrared radiometer channel, the radiance forward model takes as input the relevant cloud variables from the state vector (profiles of visible extinction coefficient α_v and N_0') and estimates of other variables (profiles of temperature, pressure, humidity, O_3 and CO_2 concentrations, as well as skin temperature and emissivity). It produces an estimate of the radiance measured by the instrument as well as the Jacobian with respect to each of the cloud variables from the state vector.

[45] The scattering and absorption properties of ice are taken from the database of *Baran* [2003], which assumes aggregates. At each radiometer wavelength λ , the ice particle distributions described in section 3.1 have been used to create look-up tables such that from an input profile of α_v and N_0^* , profiles can be calculated of extinction coefficient α_λ , single-scatter albedo \tilde{w}_λ and asymmetry factor g_λ . This is illustrated by box 7 of Figure 1.

[46] Gaseous absorption is represented using the correlated k distribution method [Fu and Liou, 1993]; the radiance code is essentially run multiple times to represent the variation of absorption coefficient within the wavelength band of a particular channel. Line-by-line calculations using the code of *Kato et al.* [1999] have been performed to determine the number of quadrature points required and to

produce the necessary look-up tables for each satellite channel of interest. The spectral features of different gases within a channel are assumed to overlap randomly. For example, for the 8.7- μm channel of the Spinning-Enhanced Visible and Infrared Imager (SEVIRI) on Meteosat, a 6-point integration is required over the H_2O spectrum and a 2-point integration over the O_3 spectrum, resulting in 12 calculations. The cloud properties are kept constant in each calculation. The final radiance and Jacobian are computed as a weighted average of the radiances and Jacobians from each individual calculation, using Gaussian Quadrature.

[47] The individual radiance calculations employ the “two-stream source function technique” of *Toon et al.* [1989], which is very fast but still represents scattering with sufficient accuracy to be used in the infrared when clouds are present. This is illustrated by box 8 in Figure 1. First, a two-stream calculation is performed to estimate the upwelling and downwelling monochromatic fluxes, F^\pm . We use the method exactly as described by *Fu et al.* [1997], in which the fluxes are effectively radiances in the directions $\pm\mu_1$ (where μ denotes the cosine of a zenith angle) and the optimal value for two-stream calculations in the infrared is $\mu_1 = 1/1.66$ [*Fu et al.*, 1997]. To account for the strong forward scattering peak in the phase function, delta scaling is applied to α_λ , \tilde{w}_λ and g_λ as described by *Joseph et al.* [1976]. A radiance calculation is then performed in the satellite direction μ , using the fluxes already calculated to estimate scattering into the radiometer field of view:

$$\mu \frac{dI(\delta, \mu)}{d\delta} = I(\delta, \mu) - c^+ F^+(\delta) - c^- F^-(\delta) - (1 - \tilde{w})B, \quad (23)$$

where δ is the delta-scaled normal optical depth of the atmosphere above the point in question, $I(\delta, \mu)$ is the radiance in direction μ , B is the Planck function at that point, and the subscript λ has been dropped for brevity. Again treating the fluxes as radiances in the directions $\pm\mu_1$, we can use the two-stream phase function [*Fu et al.*, 1997] to obtain $c^\pm = \tilde{w}(1 \pm 3g\mu\mu_1)/2\pi$. Assuming isotropic emission and scattering at the surface, the surface radiance in direction μ is related to the surface upwelling flux by $I_s = F_s^+/\pi$. The top-of-atmosphere radiance, $I(0, \mu)$, is thus calculated by numerically integrating (23) up from the surface. Comparisons with the 16-stream DISORT code (Discrete Ordinates Radiative Transfer Program [*Stamnes et al.*, 1988]) demonstrate that for zenith radiances our code is accurate to better than 1%. The development above may be easily adapted to the forward modeling of radiance differences between channels, ΔI . Details of how the Jacobian of the radiance model is calculated are given in Appendix A.

3.6. Visible Optical Depth Forward Model

[48] From the A-Train during the day, an estimate of the visible optical depth δ_v is available from the Moderate Resolution Imaging Spectroradiometer (MODIS) on board Aqua [*Platnick et al.*, 2003]. In principle, similar estimates may be made over ground-based sites using the solar channels of geostationary satellites. As discussed in section 2.1, we choose to treat δ_v as a direct measurement;

it is forward modeled simply by summing the visible extinction coefficient through the cloud column:

$$\delta_v = \sum_{i=1}^n \alpha_{v,i} \Delta z_i, \quad (24)$$

where Δz_i is the thickness of cloud layer i and $\alpha_{v,i}$ is the corresponding visible extinction coefficient. This is represented by box 9 in Figure 1. In practice, Δz_i is the width of a lidar range gate and is constant with range.

[49] The part of the Jacobian corresponding to δ_v is easy to compute: the partial derivatives of δ_v with respect to α_v are given by

$$\left. \frac{\partial \delta_v}{\partial \ln \alpha_{v,i}} \right|_{N_0^*} = \alpha_v \Delta z. \quad (25)$$

Since δ_v is independent of N_0^* and S , the partial derivatives with respect to them are zero.

[50] One of the problems of using an estimate of δ_v as if it were a direct measurement is that many assumptions are made in passive retrievals using solar radiances, particularly on the value of asymmetry parameter, and these introduce errors in the resulting estimate of δ_v . An aspiration is to forward model the solar radiances directly, which would have the advantage that the microphysical assumptions would be consistent with those made in the other parts of the retrieval, and in particular that the asymmetry parameter used in the interpretation of the solar radiances would be consistent with particle sizes inferred from the radar-lidar information.

3.7. Forward Model Error

[51] As discussed in section 2.5, it is important to include the contribution of forward model error to the observation error covariance matrix \mathbf{R} . In the case of the radar model, the leading source of error is the fact that we represent the size distribution by a single shape, as described in section 3.1. If it is assumed that the α_v and N_0^* values input to the forward model are exact, then the horizontal spread of points in Figure 2b implies a root-mean-squared random error in the modeled Z of 0.9 dB. An additional source of error is due to the use of a single density function, but this is very difficult to estimate. *Hogan et al.* [2006b] “forward modeled” Z from aircraft size distributions with the same density function as used here, and compared it to measured values by a Rayleigh-scattering radar. They found that in purely ice-phase clouds the average error in Z for an aircraft run was around 0.6 dB, although it should be stressed that this will contain substantial contributions from imperfect matching between the radar and aircraft sample volumes. A further error is due to the approximation of ice particles by homogeneous ice-air spheres, required for Mie theory to be applied. However, this only affects the regions of the cloud containing substantial numbers of particles larger than around 1 mm for a 94-GHz radar. Given these considerations we estimate the total radar model error to be around 1.1 dB.

[52] The error in the lidar forward model is dominated by the fact that a single value of the lidar ratio S is retrieved for each profile, while in reality it can vary with height. The

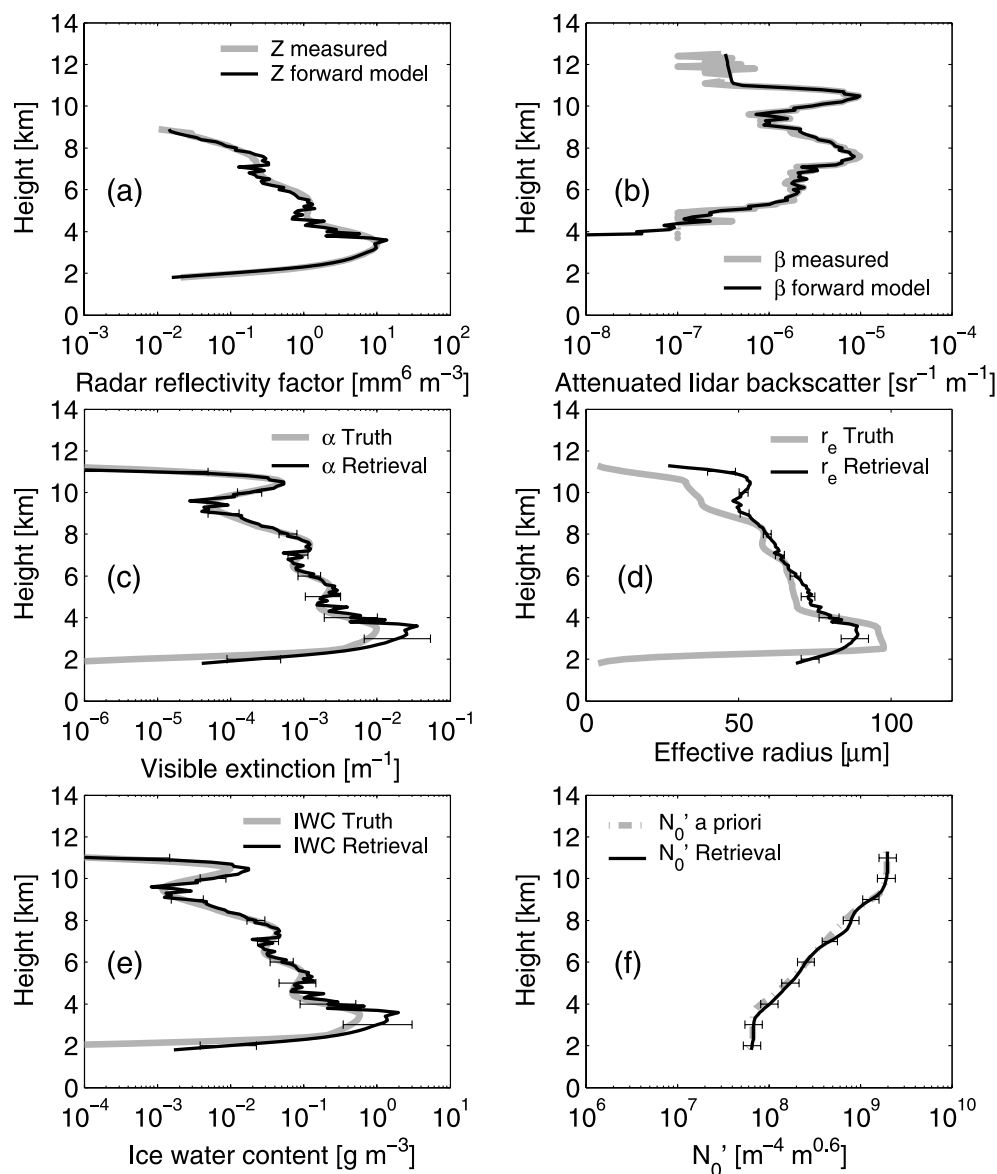


Figure 4. Demonstration of the performance of the algorithm when applied to simulated spaceborne radar and lidar measurements. The algorithm has been run without the use of infrared radiances or smoothness constraint on α_v , and the a priori error covariance matrix on N_0' is assumed to be diagonal. The gray solid lines represent the true cloud properties or the measurements, while the thin black lines with error bars are the retrieved variables or the forward model simulations at the final iteration: (a) 94-GHz radar reflectivity factor Z , (b) 532-nm apparent lidar backscatter β , (c) visible extinction coefficient α_v , (d) effective radius r_e , (e) ice water content IWC, and (f) the retrieved and a priori profiles of N_0' . The assumed observation error on Z was 1 dB and on $\ln \beta$ was the combination of a forward model error of 0.5 and the error due to photon counting statistics as described by Hogan *et al.* [2006a].

fractional error in the modeling of backscatter is therefore approximately equal to the typical fractional standard deviation of S within a profile. In section 2.2 the error in the a priori value of $\ln S$ was set to 0.5, so for consistency this value is also used for the forward model random error in $\ln \beta$. Note that the lidar model is also susceptible to errors in our ability to represent multiple scattering, but these are believed to be smaller than those due to variations in S .

[53] For the radiance model, the error includes a contribution from the error in the assumed temperature profile and the error in the assumed ice particle habit. Temperature is

typically taken from a model forecast or analysis, or in the case of some ground-based sites, from interpolating between radiosonde ascents. The stated error for the temperature provided by the European Centre for Medium Range Weather Forecasts (ECMWF) beneath CloudSat is 0.6 K [Benedetti, 2005], corresponding to an error in the radiance I of 2% (for a brightness temperature of 220 K at $\lambda = 10 \mu\text{m}$). In the case of modeling the radiance difference between two channels, ΔI , the errors in the temperature profile largely cancel. The error in modeling infrared radiances due to different particle habit assumptions were

estimated by *Cooper et al.* [2003] to be 1.5 K for I and 1 K for ΔI . An additional source of error occurs for optically thin scenes since then the skin temperature becomes important; *Morcrette* [2001] found errors of around 3 K for ECMWF forecasts of this variable over a midlatitude continental site.

[54] For the error in the optical depth model, we note that there is virtually no error associated with applying (24), so the dominant source of error is in deriving δ from shortwave radiances that are subject to 3D effects. Since δ is not used in the examples presented in subsequent section, we defer this discussion to a future paper.

[55] A further consideration is the mismatch in the size of the fields of view of the various instruments, particularly in the case of the A-Train where the CloudSat radar has a footprint of approximately 1 km through which several CALIPSO samples of 90-m width are made. *Illingworth et al.* [2000] used the method devised by *Hogan and Illingworth* [1999] to show the error associated with this mismatch is equivalent to a radar model error of only 0.1 dB, but if the centers of the radar and lidar samples were separated horizontally by 3 km then this error would increase to 2 dB.

[56] Finally it should be mentioned that some forward model errors have vertical correlations, which strictly should lead to \mathbf{R} having off-diagonal elements. Unfortunately, since these vertical correlations are almost all unknown, they have been ignored in this paper. Nonetheless, the formalism for including them in future is present in (10) and (11).

4. Tests Using Synthetic Profiles

[57] To test the algorithm, it is first applied to synthetic profiles of radar reflectivity factor and apparent lidar backscatter. Using the same methodology as “Blind test 2” in the work by *Hogan et al.* [2006a], radar and lidar profiles are simulated from the aircraft size spectra obtained during the European Cloud Radiation Experiment (EUCREX) and effects such as lidar attenuation, multiple scattering and instrument noise are included. All profiles used by *Hogan et al.* [2006a] have been tested, but for brevity only one (their profile 7) is shown here. This has been chosen as it demonstrates many of the strengths and weaknesses of the method.

4.1. Description of the Synthetic Measurements

[58] The calculation of both IWC and radar reflectivity factor is done assuming the mass- D relationship of *Brown and Francis* [1995], while α_v is obtained directly from the in situ measurements of ice particle cross-sectional area using the geometric optics approximation. All processing is the same as that done by *Hogan et al.* [2006a], except for the following changes that were made to simulate the CloudSat/CALIPSO satellites rather than the EarthCARE (Earth Cloud, Aerosol and Radiation Explorer) satellite [*European Space Agency (ESA)*, 2004]:

[59] 1. The lidar wavelength is 532 nm rather than 355 nm.

[60] 2. The lidar full-angle beam divergence and field of view are set to 0.1 and 0.13 mrad respectively.

[61] 3. Lidar multiple scattering is calculated with the *Hogan* [2006] rather than *Eloranta* [1998] code.

[62] 4. The lidar sensitivity such that the receiver is a photon counter with each photon corresponding to an apparent backscatter of $10^{-7} \text{ m}^{-1} \text{ sr}^{-1}$, and appropriate Poisson-distributed random instrument noise is added.

[63] 5. The radar pulse-response standard deviation is $\sigma_z = 210 \text{ m}$.

[64] 6. The minimum detectable radar reflectivity factor is set to -21 dBZ . Although this is worse than the actual CloudSat sensitivity, it simulates the common situation where the radar is unable to detect the top of the cloud that is detected by the lidar. Random radar instrument noise is added appropriate to the CloudSat pulse repetition frequency of 4300 Hz.

[65] The radiance for each infrared window radiometer channel of the SEVIRI radiometer is computed using the radiance forward model previously described in section 3.5. In this case, the radiance model takes as input the relevant cloud variables (profiles of α_v and N_{δ}^*) from the in situ measurements, and other variables from the US Standard Atmosphere [*McClatchey et al.*, 1972].

[66] It should be noted that the simulations use a value of S that is constant with height but is unknown to the algorithms. The reason is that the sensitivity of radar-lidar retrievals to variable S with height was already tested in some detail by *Hogan et al.* [2006a]. They found that variable S led to a retrieved α_v profile that tended to underestimate the true value in regions where S was less than the mean S of the profile, and vice versa. In terms of the retrieved optical depth (the vertical integral of α_v), there was therefore always some degree of cancellation of the errors in α_v , with underestimates at one height countering overestimates at another.

4.2. Result of Applying the Algorithm

[67] We now examine retrievals from the algorithm, and investigate the effect of the smoothness constraint, the a priori error covariances, and the infrared measurements on the performance. The gray solid lines in Figure 4 show the measured signals and the true cloud variables for “Profile 7” of *Hogan et al.* [2006a]. This case has a total optical depth of $\delta_v = 22$, and is a particular challenge for radar-lidar algorithms because the upper 2 km of the cloud (9–11 km in Figure 4b) is detected only by the lidar, while the lower 2 km (2–4 km in Figure 4a) is detected only by the radar.

[68] The retrieved variables and error bars are displayed by the thin black lines in Figure 4, for the case without the smoothness constraint on α_v (i.e., with $\kappa = 0$ in equation (8)) and without any a priori error covariances (i.e., with $z_0 = 0$ in equation (14) such that \mathbf{B} is diagonal). The retrieval assumes observational errors that are a combination of the instrumental errors used in the simulation, and the forward model errors discussed in section 3.7. It can be seen in Figures 4a and 4b that at the final iteration of the algorithm, the observations are very closely modeled, including the lidar measurement noise (except above 11 km where the signal is entirely due to molecular scattering). Figure 4c shows that α_v is reasonably well retrieved, but the noise in the lidar measurements has propagated into the retrievals. It should be stressed that this agreement is achieved despite the fact that the optical depth down to the point at which the

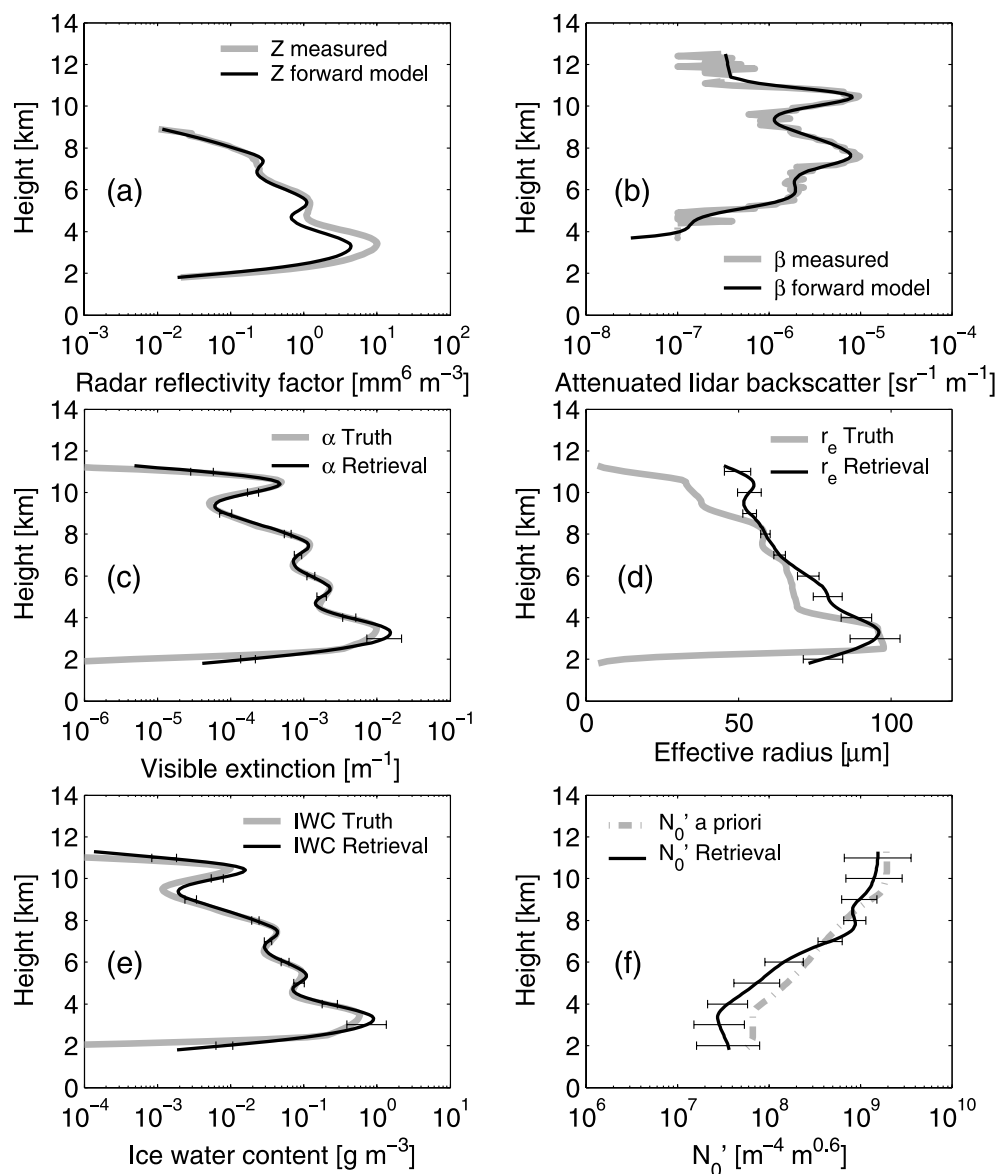


Figure 5. As Figure 4 but with a smoothing constraint on α_v and a priori error covariances for N_0' corresponding to $z_0 = 1$ km in (14).

lidar is completely extinguished is 3.5, at which point the lidar backscatter signal has been depleted to around 2.5% of its unattenuated value (accounting for the multiple scattering enhancement).

[69] Ice water content and effective radius are somewhat less accurately retrieved than α_v , in agreement with the findings of Hogan *et al.* [2006a], and are also contaminated by noise. The retrieval performs best between 4 and 9 km where both radar and lidar are available, while at the top and bottom of the cloud, the difference between retrieved and true r_e reaches $+15 \mu\text{m}$ and $-10 \mu\text{m}$ respectively. Similar errors are also present in IWC and (at the base of the cloud) in α_v , which is not surprising given the mutual dependence of these variables as shown by (19).

[70] As shown in Figure 4f, the lack of a priori error covariances results in N_0' reverting almost exactly to the temperature-dependent a priori value at cloud top and base.

Therefore we would expect the retrieved IWC in the radar-only region at cloud base to be similar to that from an empirical algorithm dependent on Z and T [e.g., Hogan *et al.*, 2006b].

[71] Next we add a smoothness constraint to α_v using a smoothness coefficient in (8) of $\kappa = 100$, as well as a priori error covariances corresponding to an error decorrelation length in (14) of $z_0 = 1$ km. The results are shown in Figure 5. It can be seen immediately that the smoothness constraint has removed all the unphysical noise from the retrieved variables. Furthermore, the a priori error covariances appear to have resulted in a more accurate retrieval of α_v , IWC and r_e at cloud base. This is because N_0' is now able to differ from the a priori value, as shown in Figure 5f, ensuring that the information in the common radar-lidar region is spread in the vertical. An intriguing aspect to this behavior is that the additional constraints prevent the

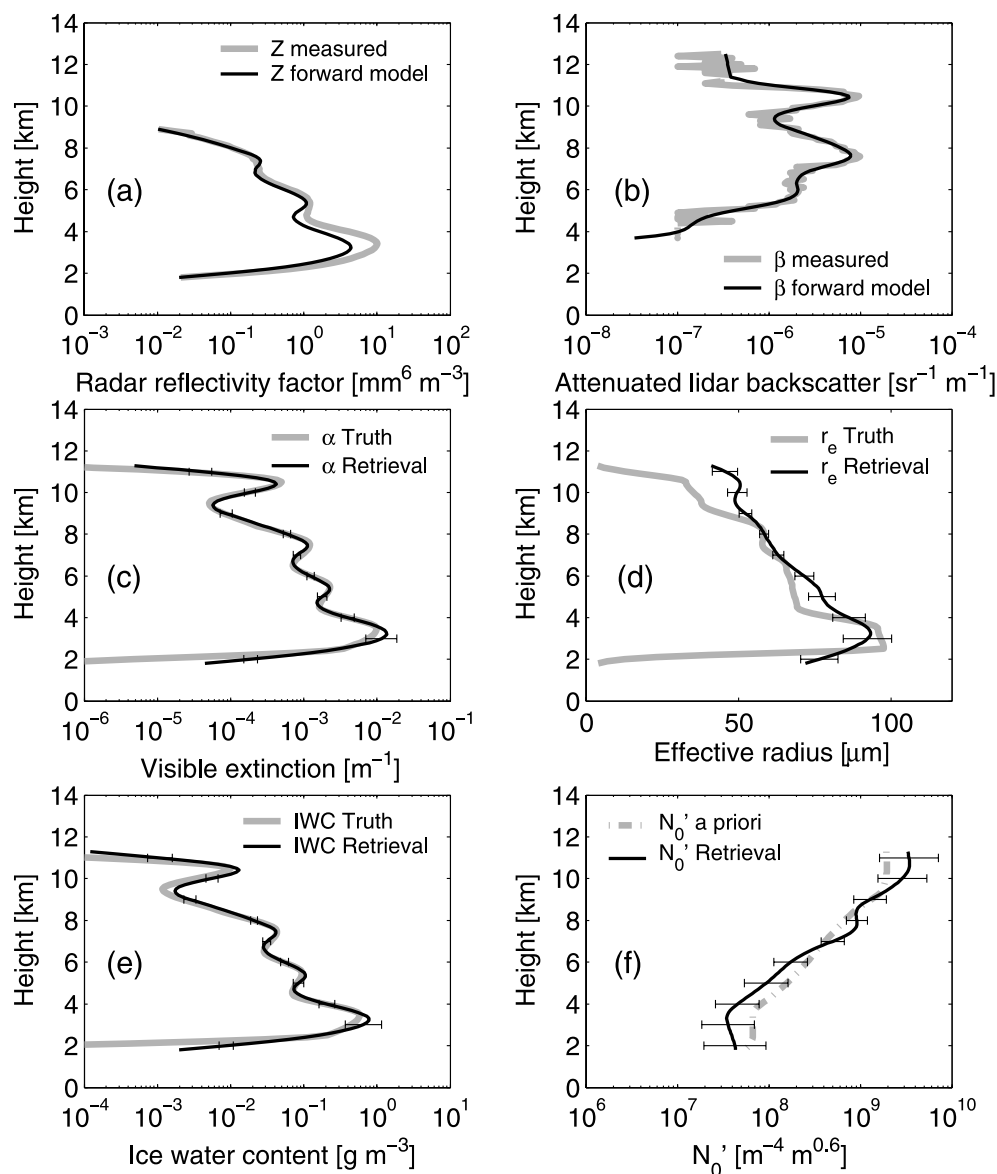


Figure 6. As Figure 5 but making use of the zenith radiance $I_{10.8}$ and the radiance difference $\Delta I_{10.8-12}$ in the retrieval process. The actual values with their assumed errors were $I_{10.8} = 7.03 \pm 0.07 \text{ Wm}^{-2} \mu\text{m}^{-1} \text{sr}^{-1}$ and $\Delta I_{10.8-12} = 0.3 \pm 0.07 \text{ Wm}^{-2} \mu\text{m}^{-1} \text{sr}^{-1}$.

algorithm from forward modeling the radar reflectivity at cloud base as accurately, even though the retrieved variables are better captured in this region.

[72] The remaining error in Figure 5 occurs at cloud top, where the cloud is detected by the lidar alone and so the only size information comes from the a priori. We therefore consider the impact on the retrieval of incorporating radiance measurements. As explained previously, zenith radiances at the top of the atmosphere I_λ are simulated with $\lambda = 10.8$ and $12.0 \mu\text{m}$. In Figure 6, the radiance at $10.8 \mu\text{m}$ and the radiance difference between channels $10.8 \mu\text{m}$ and $12.0 \mu\text{m}$ are added to the radar and lidar observations that were used in Figure 5. The main benefit of infrared radiances is in the extinction and particle size information near cloud top [Chiriaco *et al.*, 2004]. It can be seen in

Figure 5c that the cloud-top extinction retrieval without radiances was already very accurate, so the main improvement is in cloud-top r_e , where the previous overestimate has been approximately halved. In Figure 6f it can be seen that this is associated with the cloud-top N_0' no longer tending to the a priori value, but being considerably larger. We would need to conduct an analysis of the information content [Rodgers, 2000; Cooper *et al.*, 2006] to quantify objectively the contributions of the individual measurements. It should be noted that even the modest impact shown here is only achieved when the radiance error is set to 1%.

[73] To conclude this section, the capability of the algorithm to accurately retrieve cloud variables (α_v , IWC and r_e) in a simulated profile has been demonstrated even outside the part of the cloud detected by both radar and lidar. In

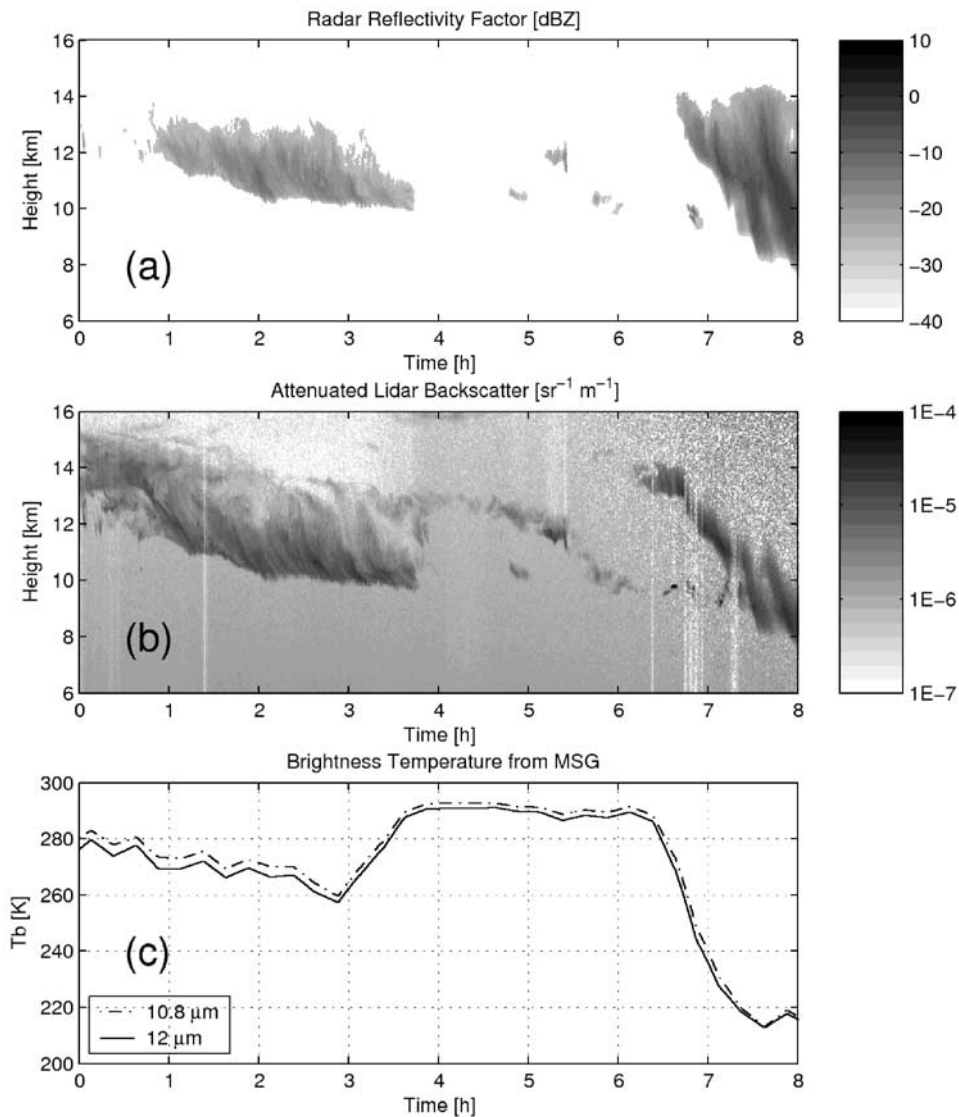


Figure 7. Observations from the ARM Mobile Facility at Niamey on 22 July 2006: (a) 94-GHz radar reflectivity factor, (b) 532-nm apparent lidar backscatter and (c) 10.8- and 12.0- μm brightness temperature measured by SEVIRI.

addition, the ability of infrared radiances to improve the retrievals at cloud top has been demonstrated.

5. Application to Ground-Based Data

[74] The method has been applied to 94-GHz cloud radar and 532-nm lidar measurements collected over Niamey in West Africa by the ARM (Atmospheric Radiation Measurement Program) Mobile Facility, as a part of the RADAGAST project [Miller and Slingo, 2007]. The data have been processed using the Cloudnet software [Illingworth *et al.*, 2007] in order to classify the targets and to correct for radar gaseous attenuation. These observations are supplemented by SEVIRI infrared radiance observations above the site from a zenith angle of 13° ($\mu = 0.97$). Temperature, pressure and humidity profiles are taken from the hourly forecasts of the ECMWF model, linearly interpolated in time, while direct

measurements of surface temperature are used in modeling the infrared radiances.

[75] Figure 7 shows time-height section through a moderately thick ice cloud observed on 22 July 2006. This case is a good illustration of the complementarity between the radar and the lidar, since the radar detected the upper part of the ice cloud between 0600 and 0800 UTC that was too thick to be penetrated by the lidar, while the first part of the cloud (0000–0400 UTC) is sampled by the lidar but only the thicker parts are detected by the radar. The 10.8 and 12.0 μm brightness temperatures observed by SEVIRI are shown in Figure 7c.

5.1. Retrievals With Only Radar and Lidar Measurements

[76] Figure 8 shows the retrieved variables when only the radar and lidar are used. Because the radar and lidar have both been averaged over 30 s, the observational error is

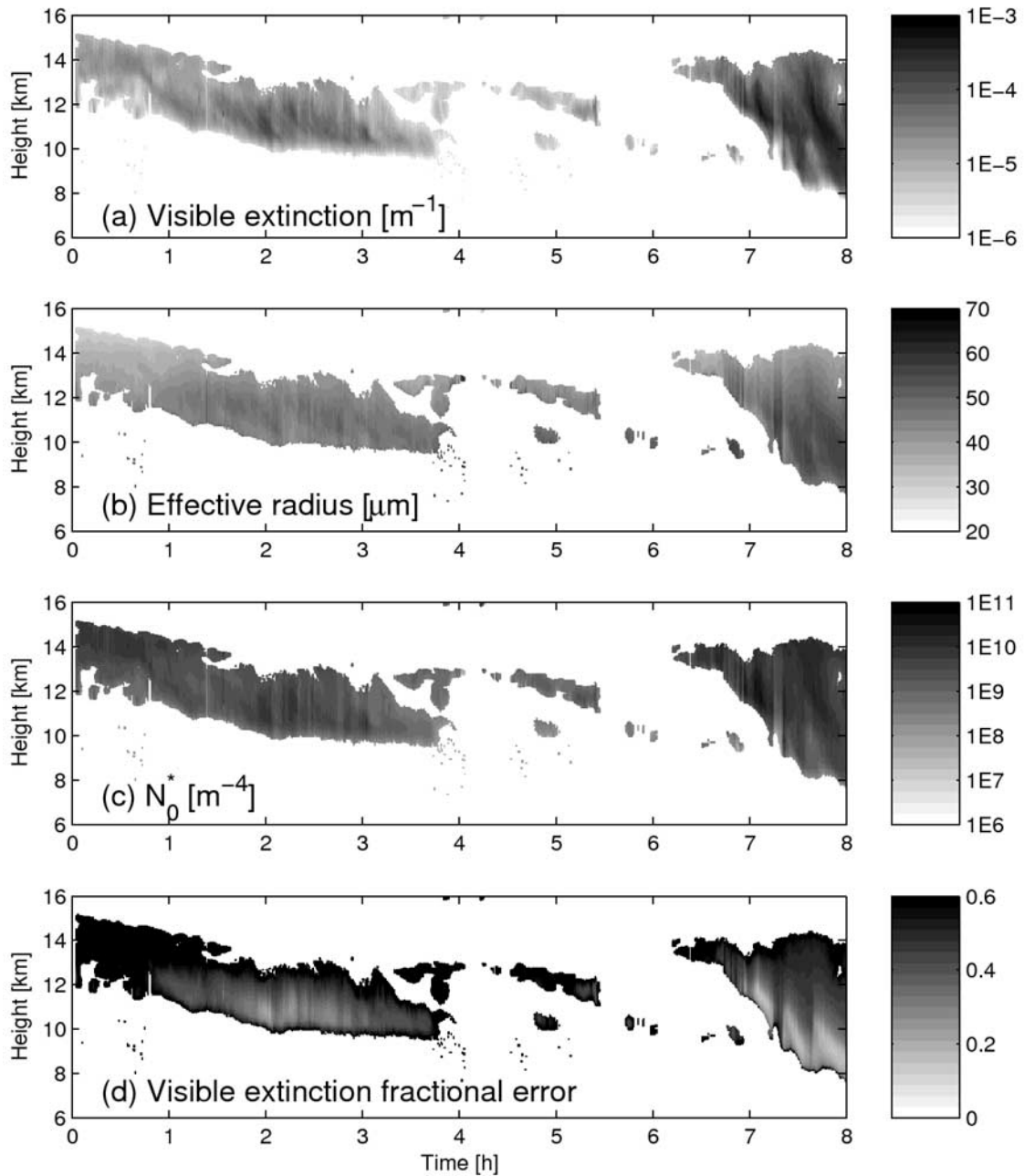


Figure 8. Retrieved variables for the cloud observed in Figure 7, using the radar and lidar observations but not the radiances: (a) visible extinction coefficient α_v , (b) effective radius r_{es} , (c) normalized number concentration parameter N_0^* , and (d) the fractional error of the visible extinction coefficient $\sigma_{\ln\alpha_v}$.

dominated by forward model error. Following the discussion in section 3.7, we assume the observational error in Z to be 1 dB and in $\ln \beta$ to be 0.5. The smoothness coefficient and decorrelation length are the same as in section 4.2 and Figure 5.

[77] The retrieved α_v is shown in Figure 8a. Although no validation data are available, it is encouraging that there are no obvious discontinuities between adjacent profiles or at

the transition between regions where both instruments detect the cloud to regions detected by only radar or lidar.

[78] Figure 8b shows that effective radius lies within the range 20 and 65 μm and tends to decrease toward cloud top, particularly toward the end of the time period (shortly before the cloud began to precipitate), although in this region the lidar only penetrates around 2 km into the cloud so most of the particle size information originates from the a priori constraint on N_0' . There are some contaminated

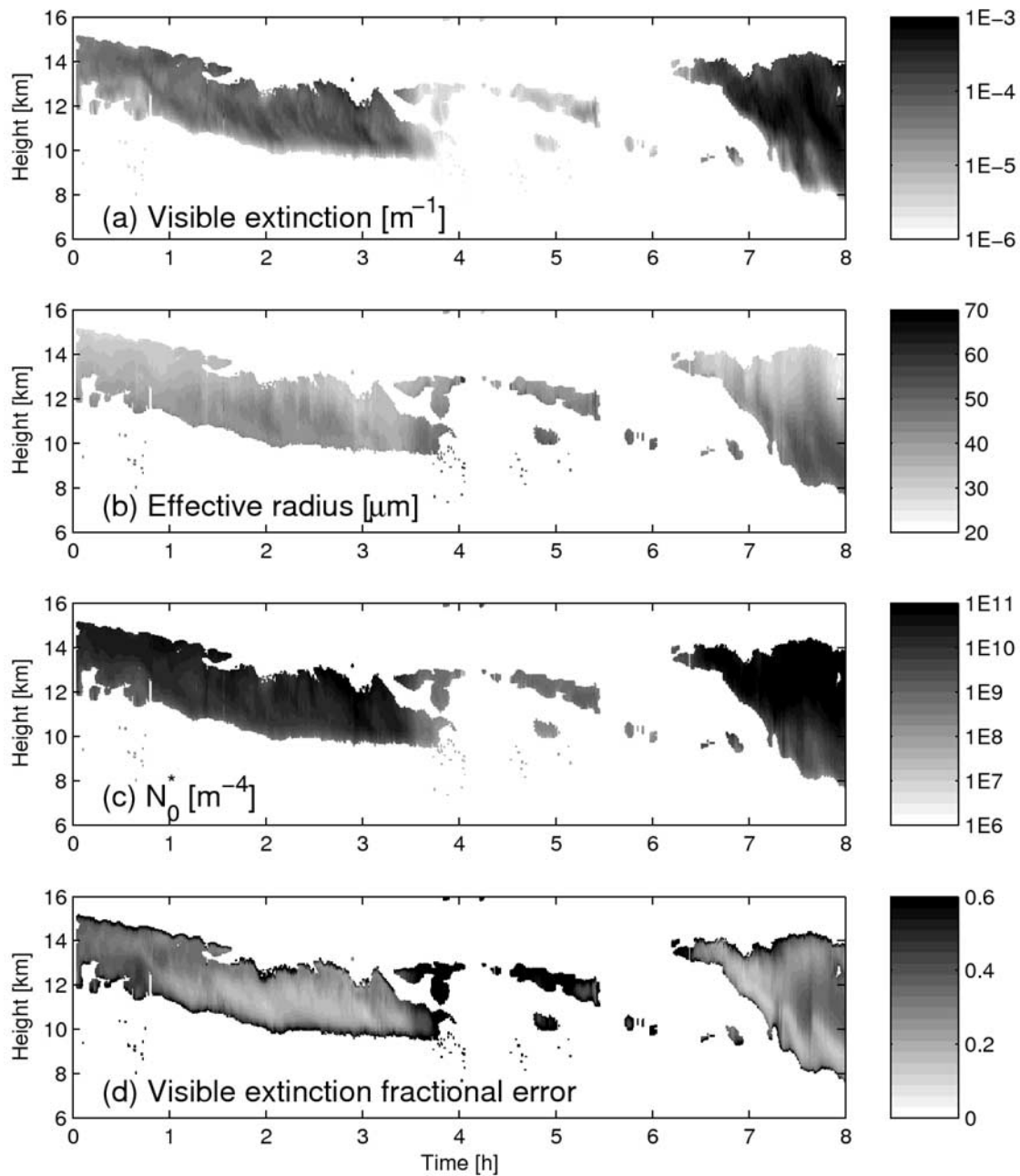


Figure 9. As Figure 8 but for a retrieval also making use of the infrared radiances.

profiles, most obviously shortly before and after 0700 UTC, where the retrieved r_e is significantly higher than in neighboring profiles. This is due to the decreased lidar backscatter in these profiles, evident in Figure 7, presumably due to attenuation by liquid water clouds below 6 km. This highlights the need to exclude profiles containing liquid water from the retrieval, or to develop a way to incorporate them into the algorithm. The normalized number concentration parameter N_0^* is shown in Figure 8c. The behavior is opposite to that of r_e in the sense that the highest values are observed near cloud top.

[79] Figure 8d shows the RMS error in $\ln \alpha_v$ (approximately equivalent to the fractional error in α_v). The error is clearly much less (typically 20–40%) in regions detected by both radar and lidar, but rises to in excess of 50% where only the radar is available and even higher in regions only detected by the lidar.

5.2. Retrievals With Radar, Lidar, and Radiometer Measurements

[80] The retrieval has been repeated but incorporating the SEVIRI radiances by forward modeling I_λ for $\lambda = 10.8 \mu\text{m}$ and ΔI for the wavelengths 10.8 and 12.0 μm . The stated

calibration performance of SEVIRI is 1 K [Schmetz *et al.*, 2002], but an additional error is due to the fact that the SEVIRI observations have been interpolated linearly between each 15-min observation time. This then needs to be combined with the model errors discussed in section 3.7. For testing purposes we assign an RMS error of 10% to the radiance corresponding to a temperature error of around 3 K for a brightness temperature of 220 K.

[81] The results are shown in Figure 9. The effect is clearly to increase α_v and N_0^* , particularly toward cloud top, while reducing r_e in this region. This implies that the radiances forward modeled by the retrievals shown in Figure 8 would significantly overestimate the observed values, and it is only by substantially increasing the cloud optical depth that agreement can be obtained. The fractional error in α_v , shown in Figure 9d appears to be much reduced because of the complementary information provided by the radiances.

[82] However, the forward modeling of radiances requires that the radar or the lidar detect all the way to cloud top. If they do not then the forward model can find itself unable to match the observed radiances because the top of the cloud is too warm, and no matter how optically thick it is, the low observed brightness temperatures cannot be modeled. This is most likely to be a problem at the top of the thick ice cloud after 0700 UTC in Figure 9, since it is known that cloud radars can have difficulty in detecting thin cirrus, particularly at a range of 15 km [Protat *et al.*, 2006]. This would explain the high α_v and N_0^* retrieved in this region. Moreover, the retrievals of extinction in Figures 8a and 9a approximately agree to within the error shown in Figure 8d, except in this particular region. We conclude that satellite radiances should be used in this way only when a lidar is available that has a clear view to cloud top. It should be noted that CloudSat and CALIPSO will be much less susceptible to this problem since CALIPSO has an unobscured view of the top of the cloud, and is believed to be able to detect even subvisual cirrus, so should easily be able to detect the clouds that contribute most to measured infrared radiances.

6. Discussion and Conclusions

[83] A new retrieval scheme has been described that combines radar, lidar and infrared radiometer measurements to retrieve profiles of the properties of ice clouds. In common with the advances made by Donovan *et al.* [2001] and Tinel *et al.* [2005], it does not need the lidar to have already been corrected for attenuation, but rather uses the radar and lidar together to find the combination of microphysical variables that best forward models the observations in a least-squares sense. This variational approach has a number of advantages over existing radar-lidar techniques, most notably the ability to include other observations and constraints, allowing the full cloud profile to be retrieved, not just the region that is detected by both radar and lidar together. Furthermore, when only a subset of the observations are available, it will automatically adopt similar behavior to existing algorithms in the literature. For example, if only the radar is available it will tend toward the reflectivity-temperature relationship of Hogan *et al.* [2006b], with radar and visible optical depth it will tend

toward the algorithm of Benedetti *et al.* [2003a], and if only lidar and infrared radiances are available it will tend toward the behavior of the method of Chiriaco *et al.* [2004].

[84] It has been tested on synthetic profiles generated from aircraft microphysical observations and on real ground-based observations, but there is clearly a need to evaluate it using simultaneous in situ aircraft observations. Work is in progress to apply it to observations from the A-Train of satellites, to be reported in a future paper.

[85] The variational framework presented here is, in principle, straightforward to expand to include both new retrieved variables (by adding them to the state vector) and new observations (by building a forward model for them). It is our aspiration to retrieve the properties of ice clouds, liquid water clouds, aerosol and precipitation within the same unified algorithm, such that all the retrieved variables are consistent with all the observations. This is counter to the current paradigm of retrieving a number of separate cloud products [e.g., Illingworth *et al.*, 2007] which each only use a subset of the available data, and often have to be run in a specific order so that a derived variable from one algorithm can be used to assist another (e.g., a liquid water content retrieval being used to correct the radar for attenuation). We envisage that the following satellite observations could be incorporated into such a unified retrieval scheme:

[86] 1. The European Space Agency is planning the launch of EarthCARE [ESA, 2004], to include a High Spectral Resolution Lidar [Shiple *et al.*, 1983] that can observe the molecular signal even within cloud. By forward modeling the molecular channel, more direct information on α_v would be obtained in the first few optical depths of the cloud, allowing the assumption of constant S to be relaxed. A similar approach could be taken for Raman lidar from the ground.

[87] 2. The EarthCARE radar will be Dopplerized, providing information of particle size via the measured fall speed [Matrosov *et al.*, 2002; Delanoë *et al.*, 2007]. By forward modeling the Doppler velocity, independent particle size information will be available and it may be possible to retrieve information on particle density.

[88] 3. Multiple field-of-view lidar provides information on cloud optical depth [Cahalan *et al.*, 2005], and with the recent development of a fast forward model for wide-angle lidar multiple scattering (Hogan and Battaglia, submitted manuscript, 2007), there is the prospect of incorporating this into a variational retrieval scheme.

[89] 4. Microwave radiances over the sea provide information on liquid water clouds and precipitation, although their use in synergy with radar and lidar may be questionable because of the much larger footprint.

[90] 5. Finally, surface echoes from the sea from both radar and lidar provide a constraint on the total attenuation and could be forward modeled directly.

[91] The use of such measurements in a variational retrieval scheme is an important precursor to directly assimilating them into models [Benedetti *et al.*, 2003b].

Appendix A

A1. Computing the Jacobian of the Radiance Forward Model

[92] To calculate the exact Jacobian for the radiance forward model as described in section 3.5 would by many

times more expensive than the radiance calculation itself. However, an approximate Jacobian may be calculated much more efficiently in the limit of no scattering. In the absorption approximation [Fu *et al.*, 1997], (23) becomes

$$\mu \frac{dI(\delta^a, \mu)}{d\delta^a} = I(\delta^a, \mu) - B, \quad (\text{A1})$$

where δ^a is the absorption optical depth. Following Fu *et al.* [1997], this has been discretized assuming exponential dependence of the Planck function on optical depth within each layer. The result is the following expression for the derivative of top-of-atmosphere radiance with respect to the absorption optical depth of layer i , δ_i^a :

$$\frac{\partial I(0, \mu)}{\partial \delta_i^a} = e^{-\delta^a/\mu} \left[\frac{B_1 e^{-\delta_i^a/\mu} - B_0}{(\mu\zeta - 1)^2} \frac{\mu\zeta}{\delta_i^a} - \frac{B_1 e^{-\delta_i^a/\mu}}{\mu(\mu\zeta - 1)} - \frac{I_{i+1}}{\mu} e^{-\delta_i^a/\mu} \right], \quad (\text{A2})$$

where B_0 and B_1 are the Planck functions for the temperatures at the top and bottom of the layer respectively and $\zeta = \ln(B_1/B_0)/\delta_i^a$. The term I_{i+1} is the radiance entering layer i from the layer below, and for increased accuracy is taken from the full two-stream source function calculation described above, rather than from the absorption approximation.

[93] Given that the absorption optical depth of the layer is related to the single-scatter albedo and infrared extinction coefficient of the clouds in the layer by

$$\delta_i^a = [(1 - \tilde{w}_i)\alpha_i + \alpha_i^{\text{gas}}]\Delta z \quad (\text{A3})$$

(where Δz is the physical depth of the layer and α_i^{gas} is the extinction coefficient of the gases), it is relatively straightforward to use the look-up tables to work out the required derivatives $\partial I(0, \mu)/\partial \ln \alpha_v$ and $\partial I(0, \mu)/\partial \ln N_0'$ at each layer.

A2. Computing the Retrieval Error in Ice Water Content and Effective Radius

[94] As outlined in section 2.5, $\mathbf{S}_{\hat{\mathbf{x}}}$ contains the error variances and covariances of the retrieved $\ln \alpha_v$, S and N_0' , with $\ln \alpha_v$ and N_0' both having n elements. In this appendix we describe how the errors and error covariances in IWC and r_e may be derived rigorously and in a way that may be easily extended to any other extensive or intensive variable. Defining column vector \mathbf{m} as:

$$\mathbf{m} = [\ln \text{IWC}_1 \cdots \ln \text{IWC}_n \ r_{e,1} \cdots r_{e,n}]^T, \quad (\text{A4})$$

the task is to compute the corresponding error covariance matrix, $\mathbf{S}_{\mathbf{m}}$. As described in section 3.1, the look-up tables can provide any variable in terms of N_0^* and the ratio α_v/N_0^* . It is therefore convenient to consider an intermediate column vector \mathbf{u} that contains these entities:

$$\mathbf{u} = \left[\ln \frac{\alpha_{v,1}}{N_{0,1}} \cdots \ln \frac{\alpha_{v,n}}{N_{0,n}} \ln N_{0,1} \cdots \ln N_{0,n} \right]^T. \quad (\text{A5})$$

This may be obtained from $\hat{\mathbf{x}}$ using $\mathbf{u} = \mathbf{U}\hat{\mathbf{x}}$, where the matrix \mathbf{U} describes how the elements of $\hat{\mathbf{x}}$ are transformed to the elements of \mathbf{u} . From (3) we derive $\ln N_0^* = \ln N_0' + 0.6 \ln \alpha_v$ and $\ln(\alpha_v/N_0^*) = 0.4 \ln \alpha_v - \ln N_0'$. Therefore, for $n = 2$, the matrix \mathbf{U} would be

$$\mathbf{U} = \begin{pmatrix} 0.4 & 0 & 0 & -1 & 0 \\ 0 & 0.4 & 0 & 0 & -1 \\ 0.6 & 0 & 0 & 1 & 0 \\ 0 & 0.6 & 0 & 0 & 1 \end{pmatrix}, \quad (\text{A6})$$

where the column of zeros in the middle corresponds to the central element of $\hat{\mathbf{x}}$ that contains $\ln S$; this is not represented in \mathbf{u} . Following (15), the error covariance matrix for \mathbf{u} is given by $\mathbf{S}_{\mathbf{u}} = \mathbf{U}\mathbf{S}_{\hat{\mathbf{x}}}\mathbf{U}^T$. The last step is to define the matrix \mathbf{M} such that we can write $\mathbf{S}_{\mathbf{m}} = \mathbf{M}\mathbf{S}_{\mathbf{u}}\mathbf{M}^T$. This matrix is similar to a Jacobian in the sense that it contains the partial derivatives of each element of \mathbf{m} with respect to each element of \mathbf{u} . The look-up tables are of the form $\text{IWC}/N_0^* = f_{\text{IWC}}(\alpha_v/N_0^*)$, or equivalently $\ln \text{IWC} = \ln N_0^* + \ln f_{\text{IWC}}(\alpha_v/N_0^*)$, where f_{IWC} represents the look-up table for IWC. Hence for $n = 2$ we have

$$\mathbf{M} = \begin{bmatrix} \frac{\partial \ln(\text{IWC}_1/N_{0,1})}{\partial \ln(\alpha_{v,1}/N_{0,1})} & 0 & 1 & 0 \\ 0 & \frac{\partial \ln(\text{IWC}_2/N_{0,2})}{\partial \ln(\alpha_{v,2}/N_{0,2})} & 0 & 1 \\ \frac{\partial r_{e,1}}{\partial \ln(\alpha_{v,1}/N_{0,1})} & 0 & 0 & 0 \\ 0 & \frac{\partial r_{e,2}}{\partial \ln(\alpha_{v,2}/N_{0,2})} & 0 & 0 \end{bmatrix}, \quad (\text{A7})$$

where the partial derivatives are simply the gradients of the look-up tables. Bringing the preceding analysis together, the error covariance of \mathbf{m} may be derived directly from the error covariance of the state vector using $\mathbf{S}_{\mathbf{m}} = \mathbf{M}\mathbf{U}\mathbf{W}\mathbf{S}_{\hat{\mathbf{x}}}\mathbf{W}^T\mathbf{U}^T\mathbf{M}^T$.

[95] **Acknowledgments.** We thank David Donovan for valuable discussions on the idea of a single unified algorithm and for computing the correlated k tables for the infrared radiative transfer code, Simone Sievert DaCosta for assistance validating the radiative transfer code against DIS-ORT, Paul Field and Chris Westbrook for very useful discussions regarding normalized particle size distributions, and Ewan O'Connor for processing the Niamey data using software developed as part of the Cloudnet project (EU contract EVK2-2000-00611). The original Niamey data were provided by the ARM Mobile Facility as part of the RADAGAST project (NERC grant NE/D002370/1). This work was supported by NERC grant NE/C519697/1. The coauthors contributed equally to this work.

References

- Ansmann, A., and D. Müller (2005), Lidar and atmospheric aerosol particles, in *Lidar Range-Resolved Optical Remote Sensing of the Atmosphere*, edited by C. Weitkamp, pp. 105–141, Springer, New York.
- Austin, R., and G. L. Stephens (2001), Retrieval of stratus cloud microphysical parameters using millimeter-wave radar and visible optical depth in preparation for Cloudsat: 1. Algorithm formulation, *J. Geophys. Res.*, *106*, 28,233–28,242.
- Baran, A. J. (2003), Simulation of infrared scattering from ice aggregates by use of a size-shape distribution of circular ice cylinders, *Appl. Opt.*, *42*, 2811–2818.
- Battaglia, A., M. O. Ajewole, and C. Simmer (2007), Evaluation of radar multiple scattering effects in Cloudsat configuration, *Atmos. Chem. Phys.*, *7*, 1719–1730.
- Benedetti, A. (2005), CloudSat AN-ECMWF ancillary data interface control document, technical document, CloudSat Data Processing Cent., Fort Collins, Colo., 16 July. (Available at http://cloudsat.cira.colostate.edu/ICD/AN-ECMWF/AN-ECMWF_doc_v4.pdf)
- Benedetti, A., G. L. Stephens, and J. M. Haynes (2003a), Ice cloud microphysics retrievals from millimeter radar and visible optical depth using an

- estimation theory approach, *J. Geophys. Res.*, 108(D11), 4335, doi:10.1029/2002JD002693.
- Benedetti, A., G. L. Stephens, and T. Vukicevic (2003b), Variational assimilation of radar reflectivities in a cirrus model—1. Model description and adjoint sensitivity studies, *Q. J. R. Meteorol. Soc.*, 129, 277–300.
- Brown, P. R. A., and P. N. Francis (1995), Improved measurements of the ice water content in cirrus using a total-water probe, *J. Atmos. Oceanic Technol.*, 12, 410–414.
- Cadet, B., V. Giraud, M. Haefelin, P. Keckhut, A. Rechou, and S. Baldy (2005), Improved retrievals of the optical properties of cirrus clouds by a combination of lidar methods, *Appl. Opt.*, 44, 1726–1734.
- Cahalan, R. F., M. McGill, J. Kolasinski, T. Várnai, and K. Yetzer (2005), THOR—Cloud thickness from offbeam lidar returns, *J. Atmos. Oceanic Technol.*, 22, 605–627.
- Chen, W.-N., C.-W. Chiang, and J.-B. Nee (2002), Lidar ratio and depolarization ratio for cirrus clouds, *Appl. Opt.*, 41, 6470–6476.
- Chiriaco, M., H. Chepfer, V. Noel, A. Delaval, M. Haefelin, P. Dubuisson, and P. Yang (2004), Improving retrievals of cirrus cloud particle size coupling lidar and three-channel radiometric techniques, *Mon. Weather Rev.*, 132, 1684–1700.
- Cooper, S. J., T. S. L'Ecuyer, and G. L. Stephens (2003), The impact of explicit cloud boundary information on ice cloud microphysical property retrievals from infrared radiances, *J. Geophys. Res.*, 108(D3), 4107, doi:10.1029/2002JD002611.
- Cooper, S. J., T. S. L'Ecuyer, P. M. Gabriel, A. J. Baran, and G. L. Stephens (2006), Objective assessment of the information content of visible and infrared radiance measurements for cloud microphysical property retrievals over the global oceans. Part II: Ice clouds, *J. Appl. Meteorol.*, 45, 42–62.
- Daley, R. (1991), *Atmospheric Data Analysis*, 457 pp., Cambridge Univ. Press, New York.
- Delanoë, J., A. Protat, J. Testud, D. Bouniol, A. J. Heymsfield, A. Bansemmer, P. R. A. Brown, and R. M. Forbes (2005), Statistical properties of the normalized ice particle size distribution, *J. Geophys. Res.*, 110, D10201, doi:10.1029/2004JD005405.
- Delanoë, J., A. Protat, J. Testud, D. Bouniol, A. J. Heymsfield, A. Bansemmer, and P. R. A. Brown (2007), The characterization of ice clouds properties from Doppler radar measurements, *J. Appl. Meteorol. Climatol.*, 46, 1682–1698.
- Donovan, D. P., A. C. A. P. van Lammeren, H. W. J. Russchenberg, A. Apituley, R. J. Hogan, P. N. Francis, J. Testud, J. Pelon, M. Quante, and J. W. F. Goddard (2001), Cloud effective particles size and water content profile retrievals using omnibeam radar and lidar observations: 2. Comparison with IR radiometer and in situ measurements of ice clouds, *J. Geophys. Res.*, 106, 27,449–27,464.
- Eloranta, E. W. (1998), A practical model for the calculation of multiply scattered lidar returns, *Appl. Opt.*, 37, 2464–2472.
- European Space Agency (2004), Earthcare—Earth Clouds, Aerosols and Radiation Explorer, *The Six Candidate Earth Explorer Missions*, Eur. Space Agency Spec. Publ., ESA SP-1279(1).
- Field, P. R., R. J. Hogan, P. R. A. Brown, A. J. Illingworth, T. W. Choullarton, and R. J. Cotton (2005), Parameterization of ice particle size distributions for mid-latitude stratiform cloud, *Q. J. R. Meteorol. Soc.*, 131, 1997–2017.
- Foot, J. S. (1988), Some observations of the optical properties of clouds—2. Cirrus, *Q. J. R. Meteorol. Soc.*, 114, 145–1647.
- Francis, P. N., P. Hignett, and A. Macke (1998), The retrieval of cirrus cloud properties from aircraft multi-spectral reflectance measurements during EUCREX'93, *Q. J. R. Meteorol. Soc.*, 124, 1273–1291.
- Fu, Q., and K. N. Liou (1993), Parameterization of the radiative properties of cirrus clouds, *J. Atmos. Sci.*, 50, 2008–2025.
- Fu, Q., K. N. Liou, M. C. Cribb, T. P. Charlock, and A. Grossman (1997), Multiple scattering parameterization in thermal infrared radiative transfer, *J. Atmos. Sci.*, 54, 2799–2812.
- Heymsfield, A. J., et al. (2008), Testing and evaluation of ice water content retrieval methods using radar and ancillary measurements, *J. Atmos. Sci.*, in press.
- Hogan, R. J. (2006), Fast approximate calculation of multiply scattered lidar returns, *Appl. Opt.*, 45, 5984–5992.
- Hogan, R. J. (2007), A variational scheme for retrieving rainfall rate and hail intensity from polarization radars, *J. Appl. Meteorol. Climatol.*, 46, 1544–1564.
- Hogan, R. J., and A. J. Illingworth (1999), The potential of spaceborne dual-wavelength radar to make global measurements of cirrus clouds, *J. Atmos. Oceanic Technol.*, 16, 518–531.
- Hogan, R. J., and E. J. O'Connor (2006), Facilitating cloud radar and lidar algorithms: The Cloudnet instrument synergy/target categorization product, Cloudnet documentation, Univ. of Reading, Reading, UK. (Available at <http://www.cloud-net.org/data/products/categorize.html>)
- Hogan, R. J., D. P. Donovan, C. Tinel, M. A. Brooks, A. J. Illingworth, and J. P. V. Poiras Baptista (2006a), Independent evaluation of the ability of spaceborne radar and lidar to retrieve the microphysical and radiative properties of ice clouds, *J. Atmos. Oceanic Technol.*, 23, 211–227.
- Hogan, R. J., M. P. Mittermaier, and A. J. Illingworth (2006b), The retrieval of ice water content from radar reflectivity factor and temperature and its use in the evaluation of a mesoscale model, *J. Appl. Meteorol. Climatol.*, 45, 301–317.
- Hollingsworth, A., and P. Lönnberg (1986), The statistical structure of short-range forecast errors as determined from radiosonde data. Part I: The wind field, *Tellus, Ser. A*, 38, 111–136.
- Illingworth, A. J., R. J. Hogan, A. C. A. P. van Lammeren, D. P. Donovan, F. H. Berger, T. Halecker, C.-L. Liu, A. Feijt, and H. I. Bloemink (2000), Quantification of the synergy aspects of the Earth Radiation Mission, final report, *ESTEC Contract 13167/98/NL/GD*, Eur. Space Res. and Technol. Cent., Noordwijk, Netherlands.
- Illingworth, A. J., et al. (2007), Cloudnet—Continuous evaluation of cloud profiles in seven operational models using ground-based observations, *Bull. Am. Meteorol. Soc.*, 88, 883–898, doi:10.1175/BAMS-88-6-883.
- Intrieri, J. M., G. L. Stephens, W. L. Eberhart, and T. Uttal (1993), A method for determining cirrus cloud particle sizes using lidar and radar backscatter techniques, *J. Appl. Meteorol.*, 32, 1074–1082.
- Joseph, J. H., W. J. Wiscombe, and J. A. Weinman (1976), The delta-Eddington approximation for radiative flux transfer, *J. Atmos. Sci.*, 33, 2452–2459.
- Kato, S., T. P. Ackerman, J. H. Mather, and E. E. Clothiaux (1999), The k-distribution method and correlated-k approximation for a shortwave radiative transfer model, *J. Quant. Spectrosc. Radiat. Transfer*, 62, 109–121.
- Liebe, H. J. (1985), An updated model for millimeter-wave propagation in moist air, *Radio Sci.*, 20, 1069–1089.
- Liu, C. L., and A. J. Illingworth (2000), Towards more accurate retrievals of ice water content from radar measurement of clouds, *J. Appl. Meteorol.*, 39, 1130–1146.
- Löhnert, U., S. Crewell, and C. Simmer (2004), An integrated approach toward retrieving physically consistent profiles of temperature, humidity, and cloud liquid water, *J. Appl. Meteorol.*, 43, 1295–1307.
- Matrosov, S. Y., B. W. Orr, R. A. Kropfli, and J. B. Snide (1994), Retrieval of vertical profiles of cirrus cloud microphysical parameters from Doppler radar and infrared radiometer measurements, *J. Appl. Meteorol.*, 33, 617–626.
- Matrosov, S. Y., A. V. Korolev, and A. J. Heymsfield (2002), Profiling cloud ice mass and particle characteristic size from Doppler radar measurements, *J. Atmos. Oceanic Technol.*, 19, 1003–1018.
- McClatchey, R. A., R. W. Fenn, J. E. A. Selby, F. E. Volz, and J. S. Garing (1972), *Optical Properties of the Atmosphere*, 3rd ed., Rep. AFCRL72-0497, Air Force Cambridge Res. Lab., L. G. Hanscom Field, Mass.
- Miller, M. A., and A. Slingo (2007), The atmospheric radiation measurement (ARM) mobile facility (AMF) and its first international deployment: Measuring radiative flux divergence in West Africa, *Bull. Am. Meteorol. Soc.*, 87, 411–412.
- Mitrescu, C., J. M. Haynes, G. L. Stephens, S. D. Miller, G. M. Heymsfield, and M. J. McGill (2005), Cirrus cloud optical, microphysical, and radiative properties observed during the crystal-face experiment: A lidar-radar retrieval system, *J. Geophys. Res.*, 110, D09208, doi:10.1029/2004JD005605.
- Morcrette, J.-J. (2001), Assessment of the ECMWF model cloudiness and surface radiation fields at the ARM-SGP site, *ECMWF Tech. Memo.* 327, Eur. Cent. for Med.-Range Weather Forecasts, Reading, UK.
- Okamoto, H., S. Iwasaki, M. Yasui, H. Horie, H. Kuroiwa, and H. Kumagai (2003), An algorithm for retrieval of cloud microphysics using 95-GHz cloud radar and lidar, *J. Geophys. Res.*, 108(D7), 4226, doi:10.1029/2001JD001225.
- Platnick, S., M. D. King, S. A. Ackerman, W. P. Menzel, B. A. Baum, J. C. Riédi, and R. A. Frey (2003), The MODIS cloud products: Algorithms and examples from Terra, *IEEE Trans. Geosci. Remote Sens.*, 41, 459–473.
- Platt, C. M. R., S. C. Scott, and A. C. Dilly (1987), Remote sounding of high clouds—4. Optical properties of midlatitude and tropical cirrus, *J. Atmos. Sci.*, 44, 729–747.
- Protat, A., A. Armstrong, M. Haefelin, Y. Morille, J. Pelon, J. Delanoë, and D. Bouniol (2006), Impact of conditional sampling and instrumental limitations on the statistics of cloud properties derived from cloud radar and lidar at SIRTa, *Geophys. Res. Lett.*, 33, L11805, doi:10.1029/2005GL025340.
- Protat, A., J. Delanoë, D. Bouniol, A. J. Heymsfield, A. Bansemmer, and P. R. A. Brown (2007), Evaluation of ice water content retrievals from cloud radar reflectivity and temperature using a large airborne in-situ microphysical database, *J. Appl. Meteorol.*, 46(5), 557–572.
- Rodgers, C. D. (2000), *Inverse Methods for Atmospheric Sounding: Theory and Practice*, 238 pp., World Sci., Hackensack, N. J.

- Schmetz, J., P. Pili, S. Tjemkes, D. Just, J. Kerkmann, S. Rota, and A. Ratier (2002), SEVIRI calibration, *Bull. Am. Meteorol. Soc.*, 83, suppl., ES52–ES53.
- Shipley, S. T., D. H. Tracy, E. W. Eloranta, J. T. Trauger, J. T. Sroga, F. L. Roesler, and J. A. Weinman (1983), A high spectral resolution lidar to measure optical scattering properties of atmospheric aerosols—I. Instrumentation and theory, *Appl. Opt.*, 23, 3716–3724.
- Stamnes, K., S. C. Tsay, W. Wiscombe, and K. Jayaweera (1988), Numerically stable algorithm for discrete-ordinate-method radiative transfer in multiple scattering and emitting layered media, *Appl. Opt.*, 27, 2502–2509.
- Stephens, G. L. (2005), Cloud feedbacks in the climate system: A critical review, *J. Clim.*, 18, 237–273.
- Stephens, G. L., et al. (2002), The Cloudsat Mission and the A-Train, *Bull. Am. Meteorol. Soc.*, 83, 1771–1790.
- Stokes, G. M., and S. E. Schwartz (1994), The Atmospheric Radiation Measurement (ARM) Program: Programmatic background and design of the cloud and radiation test bed, *Bull. Am. Meteorol. Soc.*, 75, 1201–1221.
- Tinel, C., J. Testud, R. J. Hogan, A. Protat, J. Delanoë, and D. Bouniol (2005), The retrieval of ice cloud properties from cloud radar and lidar synergy, *J. Appl. Meteorol.*, 44, 860–875.
- Toon, O. B., C. P. McKay, T. P. Ackerman, and K. Santhanam (1989), Rapid calculation of radiative heating rates and photodissociation rates in inhomogeneous multiple scattering atmospheres, *J. Geophys. Res.*, 94, 16,287–16,301.
- Várnai, T., and A. Marshak (2001), Statistical analysis of the uncertainties in cloud optical depth retrievals caused by three-dimensional radiative effects, *J. Atmos. Sci.*, 58, 1540–1548.
- Wang, Z., and K. Sassen (2002), Cirrus cloud microphysical property retrieval using lidar and radar measurements—1. Algorithm description and comparison with in situ data, *J. Appl. Meteorol.*, 41, 218–229.
- Winker, D. M., J. Pelon, and M. P. McCormick (2003), The CALIPSO mission: Spaceborne lidar for observation of aerosols and clouds, *Proc. SPIE Int. Soc. Opt. Eng.*, 4893, 1–11.

J. Delanoë and R. J. Hogan, Department of Meteorology, University of Reading, Earley Gate, P.O. Box 243, Reading RG6 6BB, UK. (j.m.e.delanoë@reading.ac.uk)